LIDAR-based detection of the post-typhoon recovery of a meso-macro-tidal beach in the Beibu Gulf, China

Article *in* Marine Geology · August 2017

DOI: 10.1016/j.margeo.2017.08.008

CITATIONS
0

READS
160

8 authors, including:

Zhenpeng Ge
East China Normal University
8 PUBLICATIONS **23** CITATIONS
SEE PROFILE

Zhi-jun Dai
East China Normal University
61 PUBLICATIONS **804** CITATIONS
SEE PROFILE

Wen Wei
East China Normal University
14 PUBLICATIONS **136** CITATIONS
SEE PROFILE

Marine Geology 391 (2017) 127–143

Contents lists available at ScienceDirect

Marine Geology

journal homepage: www.elsevier.com/locate/margo

LIDAR-based detection of the post-typhoon recovery of a meso-macro-tidal beach in the Beibu Gulf, China

Zhenpeng Ge[a], Zhijun Dai[a,b,*], Wenhong Pang[a], Shushi Li[c], Wen Wei[a], Xuefei Mei[a], Hu Huang[c], Jinghua Gu[a]

[a] State Key Laboratory of Estuarine and Coastal Research, East China Normal University, Shanghai 200062, China
[b] Laboratory for Marine Geology, Qingdao National Laboratory for Marine Science and Technology, Qingdao, 266061, China
[c] The Key Laboratory of Coastal Science and Engineering, Beibu Gulf, Qinzhou University, Qinzhou 535011, China

ARTICLE INFO

Keywords:
LIDAR detection
Beach recovery
Typhoon action
Meso-macro-tidal environment

ABSTRACT

Because of global sea-level rising with frequent storm activities, most beaches in the world experience widespread erosion, which poses a significant hazard to beach management. The morphodynamic process of the evolution of a beach in response to storm activities is of increasing concern. Using a terrestrial laser scanner, the topography of Yintan beach was continuously observed for 33 days with a 25 cm spatial resolution digital elevation model (DEM) of that covered an area of 15 ha before and after typhoon Rammasun. The short-term beach recovery was explored using a comprehensive approach, which included grey relational analysis, terrain analysis, Gaussian fitting, Gamma fitting, and Delft3D wave simulation methods. The results show that the Yintan beach recovery process can be divided into three stages with two transition points. Stage one began at the end of Rammasun, which indicated a weakly stable state with an average daily net erosion of $-588\ m^3$, a mean beach slope that ranged from 0.96° to 1.28°, and a landform with no obvious alterations. After the vast accretion of 6874 m^3 of first transition, stage two, which was characterized by oscillations, occurred in the region with an average daily net erosion of $-396\ m^3$ and a conspicuous beach slope reconstruction in the range of 0.94°–2.16°. During this stage, sandbar reconstruction played a key role. The second transition event arose at the end of stage two with a vast accretion of 5762 m^3. Afterwards, the daily net accretion of 200 m^3 and the beach slope range of 0.93°–1.74° dominated the region during stage three, and the beach surface became similar to that of the pre-Rammasun. Within the entire observation period, intense beach elevation changes that ranged from −15 cm to −6 cm and 6 cm to 15 cm mainly occurred in the sandbar and foreshore zones, respectively. Additionally, slight elevation changes (ranging from −4 cm to 4 cm) were densely distributed in the backshore and dunes, and moderate elevation changes (ranging from −6 cm to −4 cm and 4 cm to 6 cm) emerged along the entire beachface. It was concluded that the spatial distribution of the bottom shear stress that was induced by wave action was responsible for the reconstruction of the foreshore and sandbar after Rammasun, whereas the short-term beach recovery process was affected by the beach states in various wave breaking conditions.

1. Introduction

Generally, the beach acts as the first barrier of defense against wave-induced erosion and associated sea-level rises (Stive, 2004; Zhang et al., 2004; Anthony, 2008). However, due to global sea-level rising with frequent storm activity, at least 70% of sand beaches experience widespread erosion around the world (Bird, 1985). It was reported that the length of eroded beach in China is approximately 2463.4 km, which accounts for approximately 50% of total Chinese continental coastline (TIOS, 2010). Moreover, serious beach erosion with different morphodynamic states due to storms is also observed in the USA (Moore et al., 1999; Allen, 2006; Rogers et al., 2012; Psuty et al., 2013; Houston and Dean, 2014), Europe (Del Río et al., 2012; Semeoshenkova and Newton, 2015), Asia (Dai et al., 2007; Dai et al., 2010; Qi et al., 2010; Yoshikawa and Nemoto, 2010; Allenbach et al., 2015; Noshi et al., 2015), Oceania (Castelle et al., 2007; Berry et al., 2014), South America (Semeoshenkova et al., 2016) and Africa from time to time (Smith et al., 2014). Therefore, assessing the 'vulnerability' of a beach in response to storm activity is significant, especially for beach recovery after the dissipation of a storm.

The gentle beachface slope, commonly observed in *meso* (tidal range > 3 m) - macro (tidal range > 4 m) tidal environment (Short,

* Corresponding author at: State Key Lab of Estuarine & Coastal Research, East China Normal University, Shanghai 200062, China.
E-mail address: zjdai@sklec.ecnu.edu.cn (Z. Dai).

http://dx.doi.org/10.1016/j.margeo.2017.08.008
Received 19 September 2016; Received in revised form 29 July 2017; Accepted 8 August 2017
Available online 09 August 2017
0025-3227/

1991), responds to storms in various ways. Erosion, which is caused by dominant offshore sediment transport, has been intensively studied by researchers (e.g., Snedden et al., 1988; Wright et al., 1991; Conley and Beach, 2003). However, accretion, which is caused by dominant onshore-directed transport, may also occur in certain regions during storms (e.g., Hill et al., 2004; Anthony, 2013). Generally, the sediment transport direction is determined by the coupling of the wave velocity asymmetry (onshore), oscillatory infragravity wave (offshore) and undertow (offshore) (Wright et al., 1991; Russell, 1993; Conley and Beach, 2003; Aagaard et al., 2005). For this type of beach, the wave energy is usually dissipated over the wide surf zone while the swash action (runup) cannot be neglected (indistinctive in calm condition). In addition, the width of the surf zone varies for a same wave height with changing water level (Wright et al., 1979). In the coastal dunes behind a meso-macro-tidal beach, erosion also occurs in the swash, collision, overwash and inundation regimes at various water levels (tide + storm surge + wave setup) (Sallenger, 2000). Furthermore, beach and dune erosion, which depends on the storm surge and storm duration, occurs in several hours or days (Houser et al., 2015). As a result, the prominent morphological changes, which are represented by the dune scrap and offshore migration of the sandbar, are usually dramatic (Costas et al., 2005; Masselink and Van Heteren, 2014), For example, new landforms can be formed by storms, such as troughs and cross-shore channels (Sedrati and Anthony, 2007).

Even though investigations regarding meso-macro-beach erosion in response to storm activities have been conducted worldwide, an understanding of the beach recovery process after storm is limited. The recovery process of an individual beach and its ability to return to its previous or new equilibrium state (Woodroffe, 2007) is unique (Morton et al., 1994). In response to different hydrodynamic and sediment budget conditions, the recovery period may vary from days to decades (Lee et al., 1998). However, several beaches (e.g., Catalonia beach) also experienced unrecoverable destruction due to the impacts of storm activities (Jiménez et al., 2012) while the average recovery period of the barred Biscarrosse beach is only 9 days due to the cumulatively weak impact of storm clusters (Angnuureng et al., 2017). Furthermore, based on the data set of southeastern Texas coast, Morton et al. (1994) proposed the classical theory for the beach recovery stages, which indicates that the short-term beach recovery process, which varies from several weeks to one year, usually begins immediately after the storm and is characterized by foreshore steepening, berm reconstruction and a landward migration of the innermost bar. For example, several beaches in North Carolina and New Jersey recovered approximately half of the eroded sand within one day after the storm weakened. These results were based on precise leveling (Birkemeier, 1979). Wang et al. (2006) detected a re-establishing process of the beach slope and berm in relation to the width and orientation of the beach, beach properties and supply of sediment after Hurricane Ivan through continuous observation (90 days) from the Electronic Total Station. Using ARGUS video cameras, RTK-GPS and in-situ hydrologic observation, Aagaard et al. (2005) found that dissipative beaches recover faster than reflective beaches because of the intense backwash on the reflective beaches. Dune recovery begins at the stage three (Morton et al., 1994) and takes more time for dune formation and vegetation re-colonization (Duran and Moore, 2013; Duran Vinent and Moore, 2015). Recent studies further highlighted that beach resilience is dominated by the sediment transport direction, landward migration of the nearshore sandbar, dune-building vegetation expansion and aeolian transport from the foreshore to the backshore (Houser et al., 2015). Although the beach recovery process is influenced or restarted by a sequence of storms, most beaches recover after the storms in the long run (Zhang et al., 2002). However, limited studies have explored the evolution of beach morphology in detail in response to storm activities due to limited survey instruments.

To date, most previous investigations obtained topographic data (before and after storms) using contact measurement methods, such as RTK-GPS (Aagaard et al., 2005), DGPS (Suanez et al., 2012; Coco et al., 2014), and Total Station (Costas et al., 2005; Wang et al., 2006; Sedrati and Anthony, 2007). These measurement modes possibly changed the original beach surface due to the soft beach sand. Furthermore, these methods can obtain beach profiles, which reflect only large-scale geomorphological evolution because of sparse data points. Additionally, the profiles limit the overall representation of small-scale geomorphological variations. Moreover, video-monitoring techniques with good temporal resolution, have been used to observe the sequential morphological evolution of beaches (Lippmann and Holman, 1989, Salmon et al., 2007). However, the horizontal accuracy is at the decimeter or meter level and the vertical accuracy is inadequately less. When taking photos, the errors in these images are mainly produced from the inevitable geometric distortion (Brignone et al., 2012). For a detailed study of beach topography, digital elevation models (DEMs) at high spatial resolution and accuracy can be derived from a Light detection and ranging (LIDAR) system (Saye et al., 2005; Stockdon et al., 2007).

LIDAR is an active measuring technique, which directly obtains three-dimensional (3D) vector information. Compared to traditional surveying techniques, LIDAR technology has a higher spatial resolution and superior expression ability in 3D space (Schwarz, 2010). Therefore, the LIDAR technique has been widely applied to the glacier, forestry, wetland, marine debris, and archaeology research fields, among others (Houldcroft et al., 2005; Chase et al., 2012; Tang et al., 2013; Yang et al., 2013; Ge et al., 2016). Typically, LIDAR is used for observing large-scale zones with aircraft (Woolard and Colby, 2002; Montreuil et al., 2014; Houser et al., 2015; Tang et al., 2015), but the cost of airborne LIDAR is expensive (millions of dollars) and the data accuracy of airborne LIDAR (usually with a resolution of ± 10 cm) does not satisfy the requirement of short-term beach variation monitoring (daily possible changes are < 10 cm). In contrast, the terrestrial LIDAR system has high resolution, accuracy and is inexpensive, which is suitable for short-term beach recovery research. For instance, Bonte and Levoy (2015) used the terrestrial laser scanner to explore the fine changes of beach scarp geomorphology under both fair weather and stormy wave conditions. In this study, the terrain data in a typical region of Yintan beach, including beachface and dunes, were collected after a forty-year return period typhoon using a 3D laser scanner. The holistic and detailed DEMs helped reveal the short-term beach recovery process due to the impacts of Rammasun typhoon from July 18th–July 20th, 2014.

After typhoon Rammasun on Yintan beach in the Beibu Gulf, the “rapid foreshore accretion” stage of the gentle beach slope recovery was observed daily for 33 days using the terrestrial laser scanner to describe the short-term beach recovery process. The goals of this paper are: 1) to reveal the temporal features of the beach recovery process; 2) to examine the erosion/accretion degrees in various beach sections, i.e., the spatial features of the beach recovery process and 3) to explore the possible control factors of the beach recovery process.

2. Study setting and Rammasun typhoon

This research was implemented in a region within the Yintan beach, in Guangxi province, China (Fig. 1a). Yintan beach is open to the ocean and stretches almost 13 km from east to west without nearby large rivers. The coastal lagoon had been modified into a port, and most of the coastal dunes in Yintan beach have been replaced by armoring structures for the tourist industry. The − 2 m bathymetric line indicates an underwater sandbar (Fig. 1a). Additionally, an intertidal sandbar is commonly found in this region (Fig. 1b). The beachface is relatively flat with a smooth shoreline (Fig. 1a and b).

The region is controlled by diurnal tides with occasional semi-diurnal tides over 2.30 m and 5.36 m of the mean and maximum tidal range, respectively (Huang et al., 2001). Short (1991) defined macro-tidal beaches as wave-dominated systems in the meso- (> 3 m) and macro- (> 4 m) tidal ranges; therefore, Yintan is considered a meso-

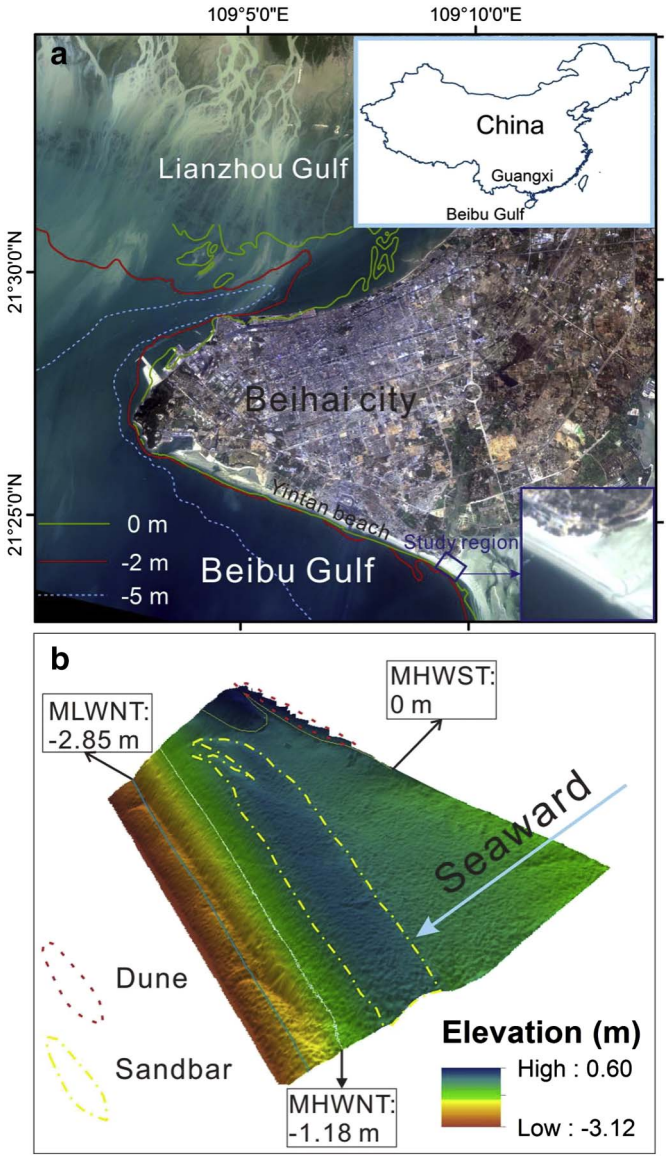

Fig. 1. (a) Satellite image of the study area. (b) Side view of study area 3D model.

macro-tidal beach. Typical water lines consist of mean high water level of neap tide (MHWNT), mean high water level of spring tide (MHWST), mean low water level of neap tide (MLWNT) and mean low water level of spring tide (MLWST), which are − 1.18 m, 0 m, − 2.85 m, and − 3.50 m in the region, respectively. The maximum wave height is usually 0.8 m in Yintan beach (Huang et al., 2001). The wave direction is N-NE during autumn and winter and SW-S during summer.

The surveyed area is characterized by a small aeolian dune with sparse vegetation. The dune has a length of approximately 77 m in the alongshore direction with an average height of 0.85 m from the foot of the dune to the dune crest. The landward side of the dune has been built with an armored structure for tourism and also because mining activity for glass making damaged the dune approximately twenty years ago. Its beachface is approximately 300 m cross-shore and 500 m along-shore. The intertidal zone exhibits a large sandbar with a seaward slope (2°–4°) steeper than the landward slope (1°), similar to the low-amplitude ridges described by Masselink et al. (2006). Moreover, ridges often emerge on the foreshore. Sediments are mainly composed of fine sand with a median size that ranges from 0.16 mm in the dune to 0.14 mm near the MLWST. Furthermore, based on the classification of Masselink and Short (1993), the studied beach is an ultra-dissipative beach characterized by dimensionless fall velocity (Ω) of 3.3 and relative tidal range (RTR) of 8.8 (Qi et al., 2010).

The Rammasun typhoon (tropical storm no. 1409) formed on July 12th, 2014 in the northwest Pacific Ocean with an initial wind speed of 18 m/s. The typhoon moved northwest from the Pacific Ocean to China and Vietnam with a minimum central pressure of 899.2 hPa. The peak wind speed reached 72 m/s in the Beibu Gulf on July 18th, 2014. Rammasun was the most violent typhoon that affected Yintan beach in the past forty years (Figs. 2 and 3) and passed over the beach from 18th to July 20th with an average speed of approximately 50 m/s. Rammasun disappeared on July 22nd, 2014. Due to the impact of Rammasun, there was an obvious storm surge with a mean and a maximum amplitude of over 0.7 m and 1.7 m, respectively. The maximum water level during the typhoon was − 0.68 m in Yintan beach (Fig. 4).

3. Data collection and methods

3.1. Data collection

In July and August of 2014, the daily maximum wave height and hourly water level were collected from a buoy, which was 30 km from the research area with a water depth of approximately 24 m. The maximum wave heights were measured at 8 am, 11 am, 1 pm, and 5 pm and their mean value represented the daily maximum wave height. Wave and water level data were obtained from the China Oceanic Information Network (http://www.coi.gov.cn/). To capture topographic changes of Yintan before and after Rammasun, daily measurements were conducted from July 17th to August 22nd, except for the 18th, 19th, and 22nd of July due to continual rainfall disturbance.

The 3D terrestrial laser scanner (RIEGL-VZ4000) (http://www.riegl.com/uploads/tx_pxpriegldownloads/DataSheet_VZ-4000_2015-03-24.

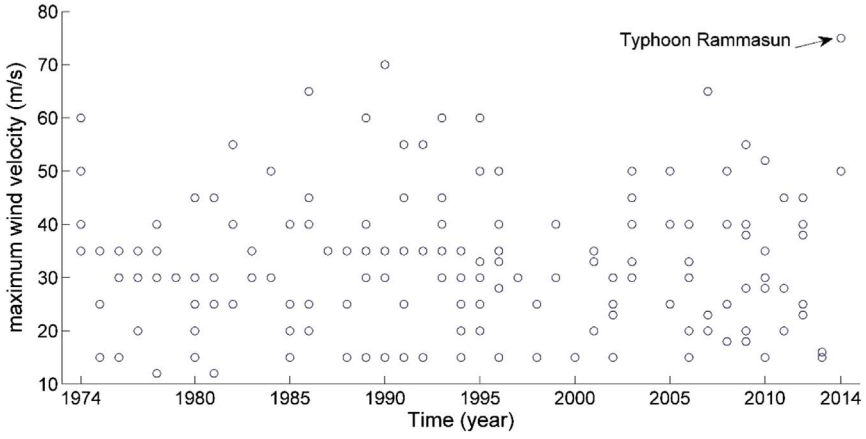

Fig. 2. The maximum wind velocity of typhoons from 1974 to 2014.

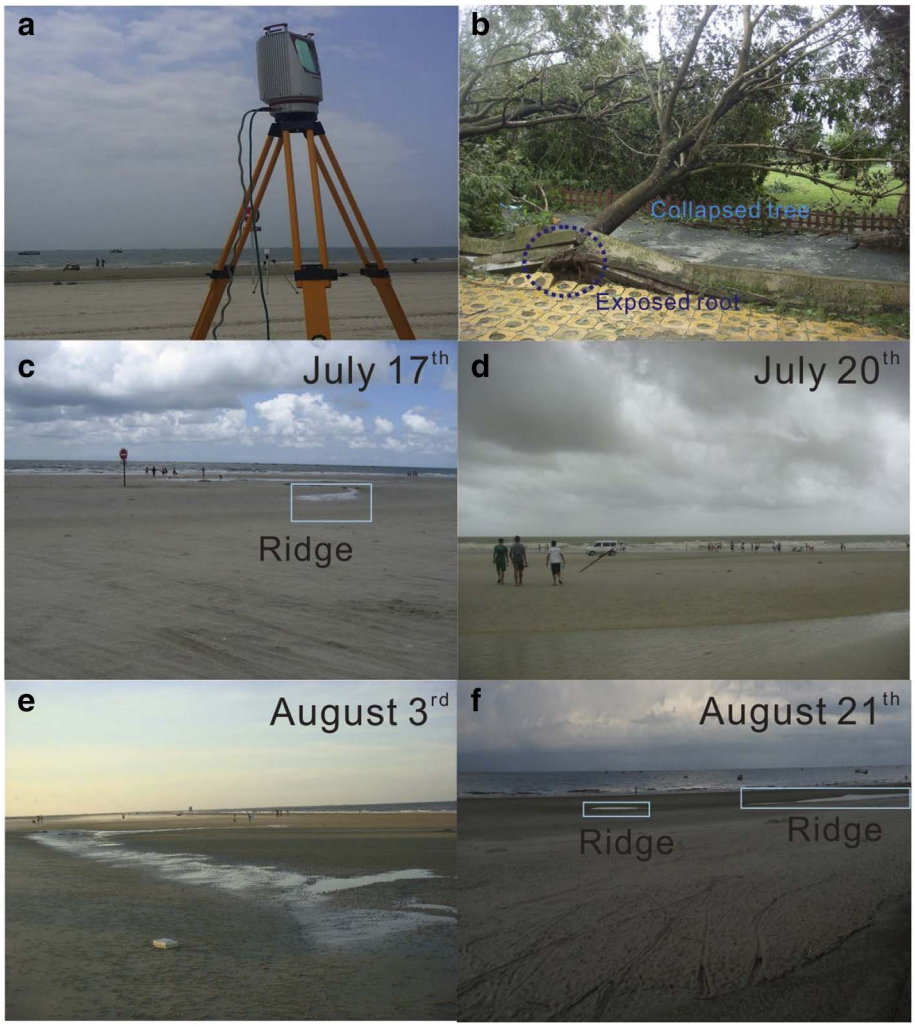

Fig. 3. LIDAR survey and tracked photos after typhoon Rammasun. (a) Laser deployment; (b) fallen tree after typhoon Rammasun (c) July 17th, one day before the typhoon; (d) July 20th, one day after the typhoon; (e) August 3rd, fifteen days after the typhoon; (f) August 21st, thirty-three days after the typhoon.

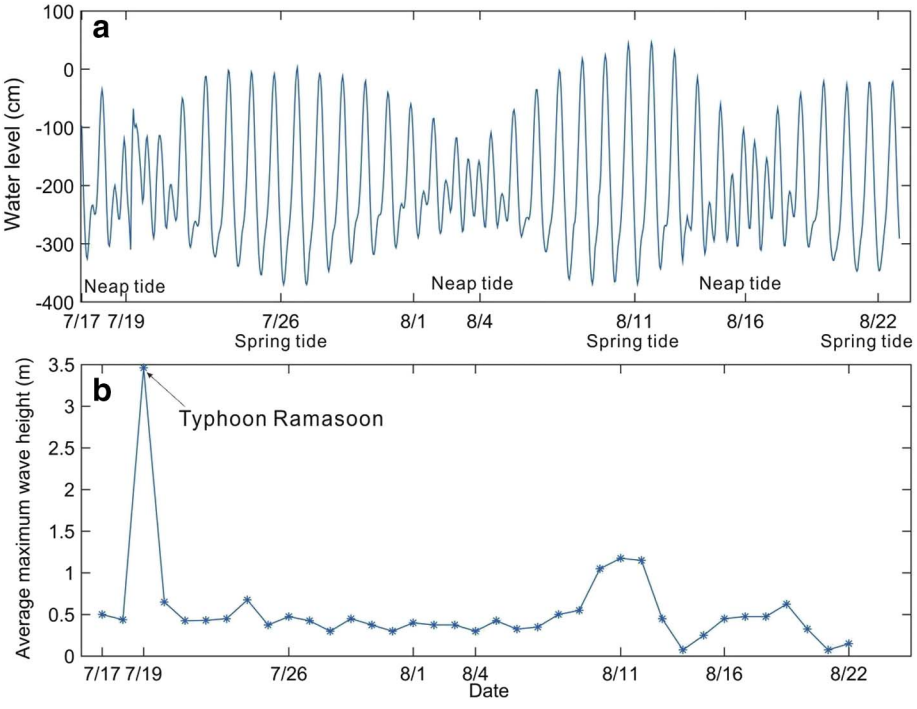

Fig. 4. Water level and average maximum wave height during the observation period. (a) Hourly water level. The x labels mean the 0 o'clock of each day (e.g. "7/1" means 00:00:00, July 1st); (b) daily average maximum wave height.

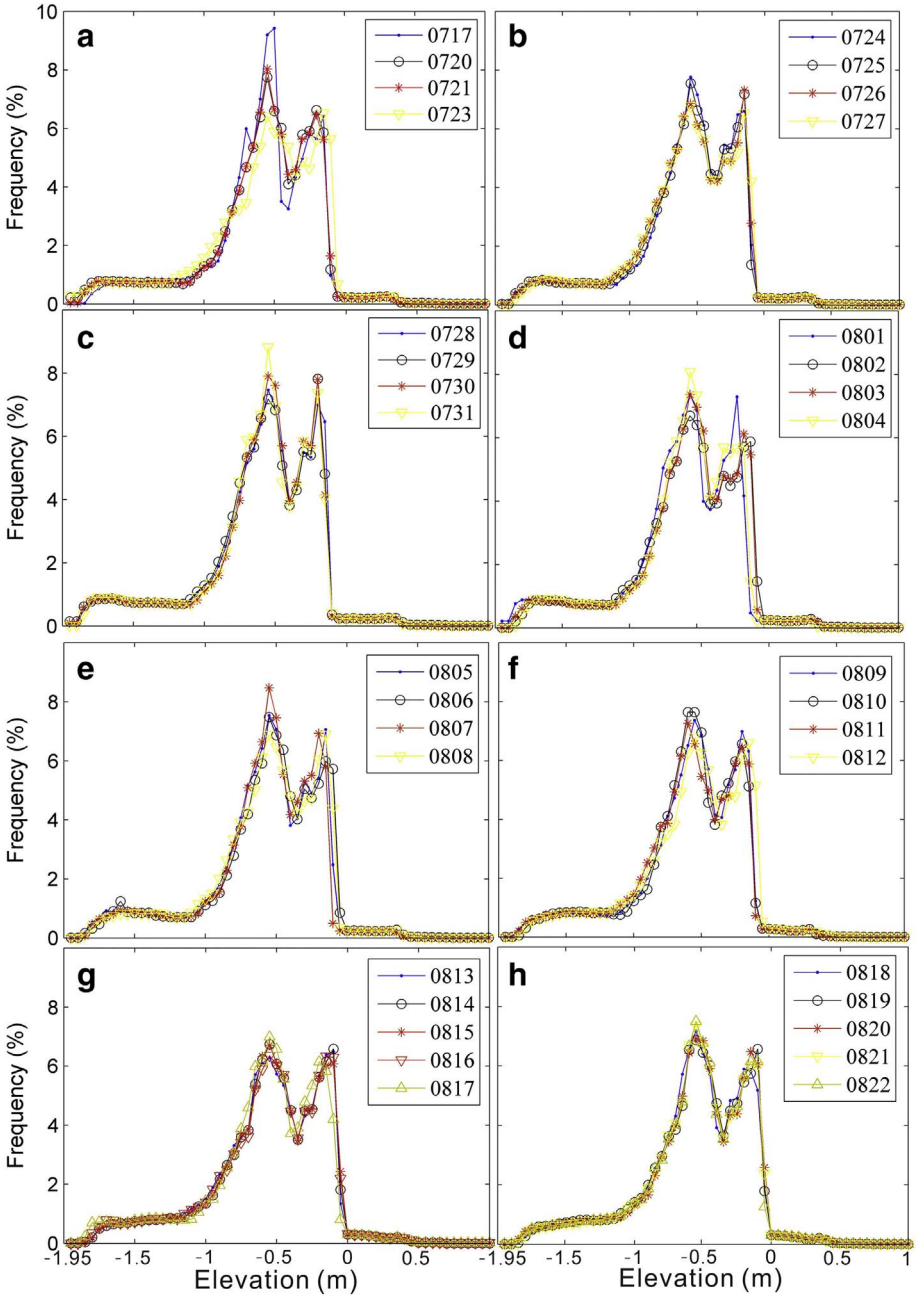

Fig. 5. The daily beach elevation frequency distributions.

pdf) operated at 200 kHz (Fig. 3a) in an area of approximately 15 ha. The laser spot size changed from 18 mm (near the laser scanner) to 75 mm (500 m away from the laser scanner). To guarantee the accuracy and point density of the data, only the points within 150 m of laser scanner were used. Three scan positions were set everyday with one position for scanning the dunes and backshore (10 min everyday) and the other two positions for scanning the foreshore (6 min per scan position everyday). Moreover, in the first scan position, seven reflectors were finely scanned to convert the instrument coordinate system to the Beijing54 coordinate system and national height datum 1985. The central point of the reflectors was measured with the Electronic Total Station NTS-342R10A (http://www.southsurvey.com/) in non-prism mode. The two scan position data were adjusted based on the first scan position data with fixed surface features in the RISCAN PRO software. In this study, possible errors (root-mean-square error, rms) originate from the laser scanner, Electronic Total Station, the conversion of the coordinate system, and the adjustment in the two scan position data. During the observation, the maximum errors of the latter two are ± 3.1 mm and ± 2.2 mm, respectively. The error of the terrestrial laser scanner increases with distance from the scan position. In our field experiments, the error of the laser scanner is about ± 18 mm (at a maximum distance of 150 m away the laser scanner), whereas the error of the Electronic Total Station was approximately ± 2 mm. The average measuring error (rms) was approximately ± 20 mm and ranged from ± 12 mm around the scan position to ± 25 mm at the edge, so the confidence interval of the elevation changes ranges from − 4 cm to 4 cm, and this confidence interval is defined as slight beach elevation changes, what means this kind of elevation changes are too small to be accurately detected. Moreover, the mean point density is about 516 points/m^2. Through the point-cloud dataset, DEMs of the research area, with a high spatial resolution of 25 cm were obtained. Daily measurements were conducted during the low tide period at night because the laser scanner was not available for underwater topography measurement. Daily data of beach topography were acquired at the

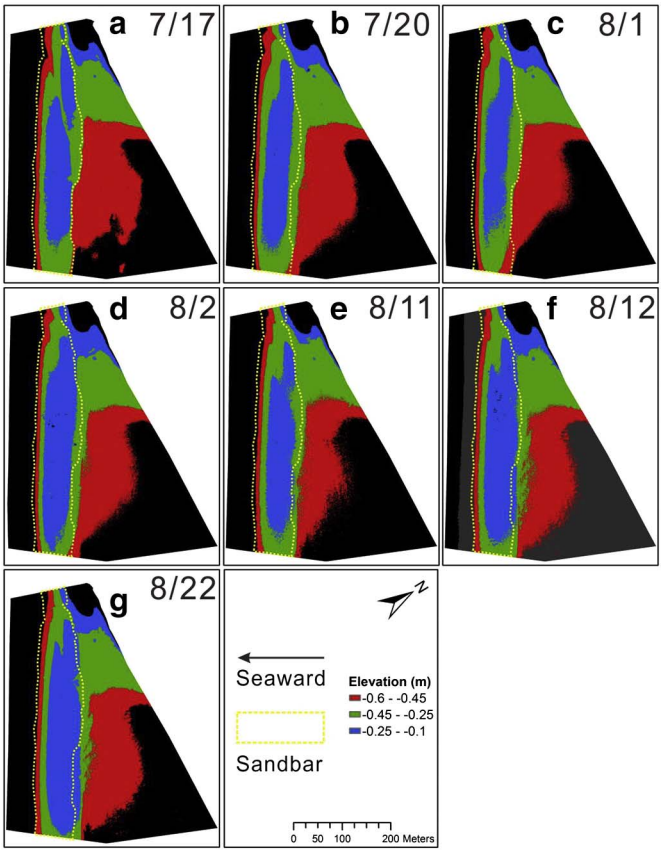

Fig. 6. The regions of two peaks and one trough in the EFD on (a) July 17th, (b) July 20th, (c) August 1st, (d) August 2nd, (e) August 11th, (f) August 12th, (g) August 22nd.

beginning of each day, what means the everyday beach topography is the pridian of the dynamic action (for instance, the beach topography of August 1st was obtained at 00:42, and the beach topography of August 2nd was obtained at 01:21, therefore, the DEM differences between August 1st and August 2nd come from the topographical changes occurring in August 1st). In this study, the plane coordinates system was Beijing 54, and the vertical datum was the national height datum 1985. Data processing were conducted using RISCAN PRO 1.7.8 (www.riegl.com), ArcGIS 10.1 and MATLAB 2012a software packages.

3.2. Methods

Based on the high spatial resolution DEMs, the elevation frequency distribution (EFD) of the beach surface with different classes was statistically calculated. To detect the beach recovery process after Rammasun, the grey relational analysis (GRA) method was used to compute the similarity between pre- and post-Rammasun EFDs.

The GRA technique, which belongs to the grey systemic analysis method, began in 1995 (Tang et al., 1995) and has been frequently used in recent years (Ip et al., 2009; Lee and Lin, 2011; Xu et al., 2011). The basic idea of GRA is the comparison in the shape of different curves to a reference curve. The more similar the shape of the curve to the reference curve, the larger the grey relational grade (GRG). The grey relational grade can be calculated as follows:

$$\Delta_{0i}(k) = \|x_0(k) - x_i(k)\| \tag{1}$$

$$\Delta_{min} = min_i min_k(\Delta_{0i}(k)) \tag{2}$$

$$\Delta_{max} = max_i max_k(\Delta_{0i}(k)) \tag{3}$$

$$\xi_{0i}(k) = \frac{\Delta_{min} + \rho\Delta_{max}}{\Delta_{0i}(k) + \rho\Delta_{max}} \tag{4}$$

$$\xi_{0i} = \frac{1}{n}\sum_{k=1}^{n}\xi_{0i}(k) \tag{5}$$

$k = 1, 2...n\ i = 1, 2...m$

where $x_0(k)$ is the EFD before Rammasun (July 17th), $x_i(k)$ is the EFD after Rammasun, $\Delta_{0i}(k)$ is the difference in absolute values between $x_0(k)$ and $x_i(k)$, Δ_{min} is the smallest value of $\Delta_{0i}(k)$, Δ_{max} is the largest value of $\Delta_{0i}(k)$, $\xi_{0i}(k)$ is the grey relational coefficient at every point, ξ_{0i} is GRG of the curve, m is 32 (32 days of data after Rammasun), and n is 60 since the sample interval was set as 5 cm in this research.

Moreover, DEMs subtractions between two consecutive days were utilized to compute the erosion and accretion in the research region. In principle, the differences in the DEMs between two adjacent days were obtained. The erosion and accretion frequency distributions were generated with a 1 cm sample interval from − 15 to 15 cm. Benefiting from the high spatial resolution, 2.68×10^6 samples were available for statistical analysis.

Using DEMs and ArcGIS 10.1 software, the aspect and slope of each DEM cell were computed. The aspect identifies the downslope direction of the maximum rate of change in the value of each cell to its neighbors, whereas the slope is the maximum rate of change in the value of each cell to its neighbors. Basically, the maximum change in elevation over the distance between the cell and its eight neighbors identifies the steepest downhill descent from the cell. Then the frequency distribution of slope can be obtained based on the statistics interval of 0.2 from 0° to 11°, whereas the aspect statistics follow the navigation frame.

The generalized Gaussian function with a least-square method was applied for fitting sediment erosion and accretion in all observed points. The generalized Gaussian function is:

$$y = f(x \mid a_j, b_j, c_j) = \sum_{j=1}^{n} a_j \exp\left(-\frac{(x - b_j)^2}{c_j^2}\right) \tag{6}$$

where a_j is the maximum value of the Gaussian distribution, b_j is the x-coordinate of the maximum value of the Gaussian distribution, c_j is the standard deviation of the Gaussian distribution, n is the number of the best fitting Gaussian function, and n varies from 1 to 3 in this research and is based on the fitting accuracy with the original values.

Gamma fitting was used for daily slope data with the method of maximum likelihood. The probability density function is:

$$y = f(x \mid a, b) = \frac{1}{b^a \Gamma(a)} x^{a-1} e^{-\frac{x}{b}} \tag{7}$$

where $\Gamma(a)$ is the gamma function that was evaluated at a, a is the shape parameter, and b is the scale parameter. After obtaining a and b, the entropy of slope system was computed by:

$$H(X) = a + \ln(b) + \ln(\Gamma(a)) + (1 - a)\psi(a) \tag{8}$$

To explore the spatial occurrence probability of various erosion/accretion groups (ranges from − 15 cm to − 6 cm, − 6 cm to − 4 cm, − 4 cm to 0 cm, 0 cm to 4 cm, 4 cm to 6 cm, 6 cm to 15 cm) during the recovery process (from July 20th to August 22nd), the events of the various groups were counted based on the pixel scale from 32 erosion/accretion rasters. Then, the counted results of different erosion/accretion groups were shown as the regional features of the beach recovery process.

To explore the impact of wave, the wave parameters (e.g., significant wave height, mean wave period) of the entire region were computed using Delft3D software (https://oss.deltares.nl/web/delft3d/). The required input parameters in the model were set according to the local environment settings. Then the bottom shear stress was obtained using the following expressions (Doucette, 2000; Masselink and Pattiaratchi, 2000; Fagherazzi et al., 2006):

$$\tau_b = \frac{1}{2}\rho f_w u_m^2 \tag{9}$$

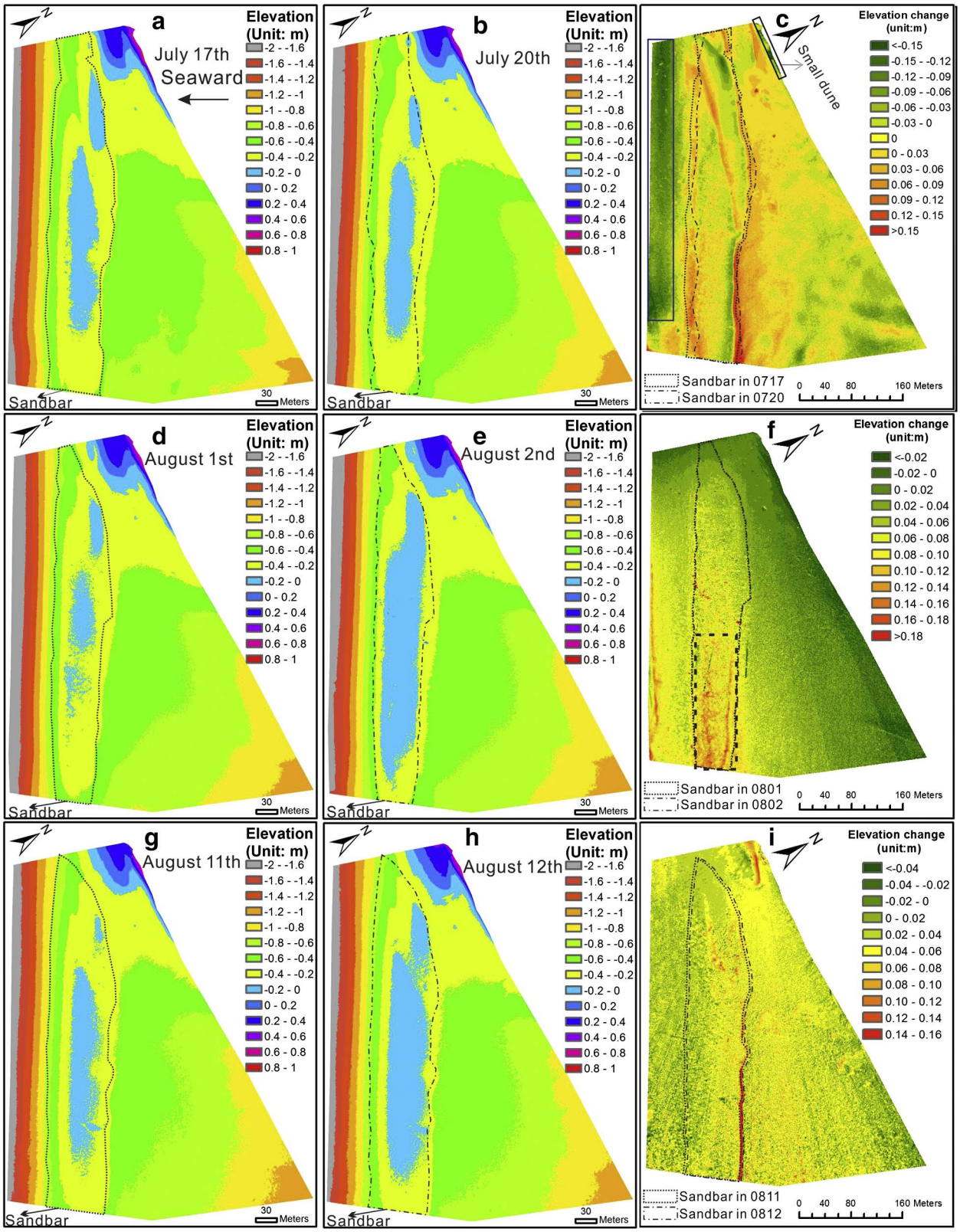

Fig. 7. DEMs of July 17th (a), July 20th (b), August 1st (d), August 2nd (e), August 11th (g) and August 12th (h). (c), (f) and (i) are the results of raster subtraction between (b) and (a), (e) and (d), (h) and (i), respectively. (c) is the elevation change caused by the typhoon, and (f) and (i) correspond to the first and second extreme accretion events, respectively.

$$u_m = \frac{\pi H}{T \sin h(kh)} \tag{10}$$

$$f_w = 1.39\left[\frac{u_m T}{2\pi (D_{50}/12)}\right]^{-0.52} \tag{11}$$

here, τ_b is the bottom shear stress, ρ is the water density, f_w is a friction factor, u_m is the maximum horizontal orbital velocity, H is the

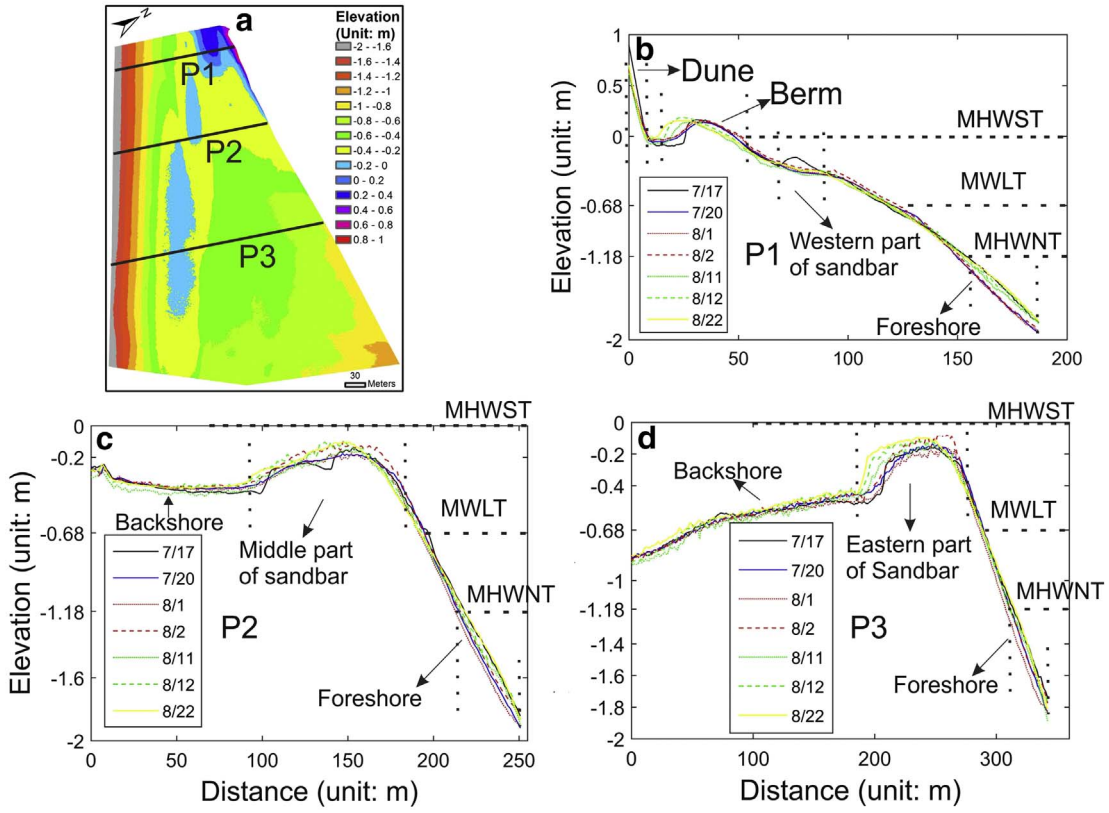

Fig. 8. Three beach profiles extracted from the DEMs. (a) Locations of the three profiles on the beach, (b) Profile P1, (c) Profile P2, and (d) Profile P3. MHWST indicates the mean high water level of spring tide; MHWNT denotes the mean high water level of neap tide; MWLT indicates maximum water level in typhoon.

significant wave height, T is the wave period, k is the wave number, h is the water depth, and D_{50} is the median size of the sediment.

Moreover, Masselink and Short (1993) proposed a beach state index (the relative tidal range (RTR)) to describe the tidal influence on the beach with a dimensionless fall velocity (Wright and Short, 1984). This index reflects the swash, surf and shoaling functions at various time scales and space:

$$RTR = TR/H_b \tag{12}$$

$$\Omega = H_b/(\omega_s T) \tag{13}$$

where TR is the tidal range, H_b is the breaking wave height, ω_s is the sediment fall speed, and T is the wave period. According to Masselink and Short (1993), the tidal range is the mean spring tidal range, but the daily tidal range was used in this work because the beach state may vary with tidal range. During the observation period, Ω was always larger than 10, so the study area is a dissipative beach, and only RTR was used in this study.

4. Results

4.1. Variations in hydrodynamic condition

The hourly water levels and daily average maximum wave heights are shown in Fig. 4. During the survey period, the beach went through two and a half lunar tidal cycle (Fig. 4a). The minimum water level was − 372 cm on July 27th, and the maximum water level was 48 cm on August 11th (national height datum 1985). Before Rammasun, the maximum wave height varied from 0.3 to 0.9 m with a peak wave period that varied from 1.6 to 3.5 s. The dominant wave direction was S and SW. During Rammasun, the maximum wave height varied from 2.5 m to 3.5 m and the peak wave period varied from 4.9 to 6.3 s. Related weak wave energy conditions were induced during Rammasun because the beach is located in a semi-sheltered gulf (Fig. 1). The dominant wave direction was S (Fig. 4a and b). After Rammasun dissipated, the maximum wave height drastically declined with a range from 0.2 m to 1.3 m and the peak period dropped from 1.8 to 3.8 s. The dominant wave direction recovered to the pre-Rammasun condition. In the subsequent days from July 20th to August 22nd after Rammasun, the average maximum wave height was < 0.5 m in most cases (Fig. 4b). Since the significant wave height was less than the maximum wave height, this beach exhibited the usual low-energy wave conditions (Doucette, 2000). Additionally, the wave condition was relatively stable in the subsequent twenty days after Rammasun. However, there were a few high-energy and super-low wave conditions (Fig. 4b) that followed tide cycle variations since August 10th (Fig. 4a and b).

4.2. Distribution of beach elevation

In Fig. 5, the beach elevation frequency distributions were mainly located in the interval of − 0.8 to − 0.05 m. Additionally, there were always two crests and one trough in the EFD of the daily DEM. Specifically, the two crests were located in the interval of − 0.6 m to − 0.45 m and − 0.25 m to − 0.1 m and the trough was located in the interval of − 0.45 m to − 0.25 m. The above three zones were roughly located between the MHWNT and MHWST. Fig. 6 shows that the first crest (from − 0.6 m to − 0.45 m) was mainly on the eastern backshore; the second crest (from 0.25 m to − 0.1 m) was located in the sandbar zone, and the trough (from − 0.45 m to − 0.25 m) was positioned between the above two areas.

After Rammasun, the frequency contribution of first crest decreased approximately 1.5%, whereas that of the trough increased by approximately 1%. Moreover, the peak of the second crest moved slightly left (Fig. 5a). As Rammasun passed, the first crest (red zone in Fig. 6) expanded in the southeast direction, whereas the two separate regions of the second crest (blue zone in Fig. 6) merged together. Additionally, the trough (green zone in Fig. 6) clearly became larger. From July 20th

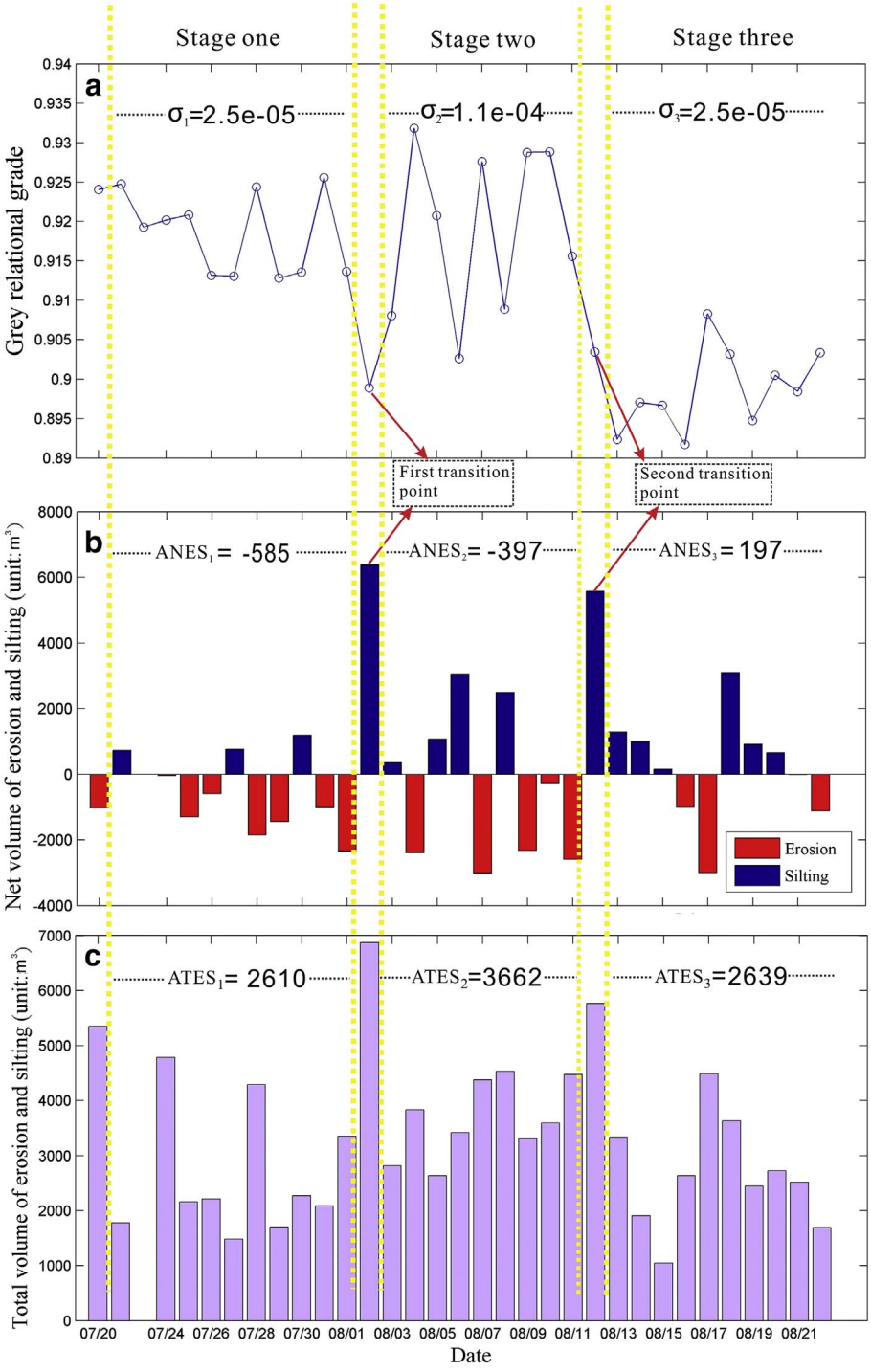

Fig. 9. Three stages of the short-term beach recovery. (a) Daily grey relational grade results; σ_i (i = 1, 2, 3) represents the variance of the grey relational grade in each phase. (b) The results of the daily net volume of erosion and accretion; $ANEA_i$ (i = 1, 2, 3) means average daily net volume of erosion and accretion. (c) The results of the daily total volume of erosion and accretion; $ATEA_i$ (i = 1, 2, 3) means average daily total volume of erosion and accretion. The first special note is that the x-coordinate "7/20" is "7/20–7/17" for both of (b) and (c). The second special note is that the erosion and accretion of (b) and (c) occurred in the previous days. For example, the beach topography of August 1st was obtained at 00:42, and the beach topography of August 2nd was acquired at 01:21, therefore, the DEM differences between August 1st and August 2nd come from the topographical changes occurring in August 1st (see Section 3.1).

to August 1st, the EFDs did not show drastic changes: however, an obvious variation was exhibited on August 2nd. Specifically, the second crest of August 2nd moved right compared with the EFD of August 1st (Fig. 5a, b, c and d), which is consist with the expansion of the blue zone in Fig. 6c and d. From August 3rd to August 11th, the moderate changes in the EFDs indicated no obvious trend; however, there was a clear trend of the entire EFD that moved right on August 12th (Fig. 5d, e and f). Clearly, the two crests on August 12th (blue zone and red zones in Fig. 6e and f) have notable extensions compared with those on August 11th. From August 13th to August 22nd, only a few changes occurred in the EFDs (Fig. 5g and h). The blue, red and green zones on August 22nd are similar to those on August 12th (Fig. 6f and g).

4.3. Variations in the beach geomorphology

4.3.1. Typhoon impact

Typhoon Rammasun dramatically modified the beach surface. For instance, on July 17th, there was a ridge on the foreshore (the cyan box in Fig. 3c), with two sandbar crests surrounding it. After Rammasun, collapsed trees with exposed roots were common behind the seawall (Fig. 3b). On July 20th, the beachface looked like a flat plain because it was hard to observe ridges and sandbars with naked eyes (Fig. 3d). From the LIDAR dataset, although most of the measured region presented an alternation between slight erosion and accretion (ranging from -2 cm to 2 cm), there was severe erosion (< -6 cm) on three zones (Fig. 7a, b and c). The most serious erosion occurred in a small

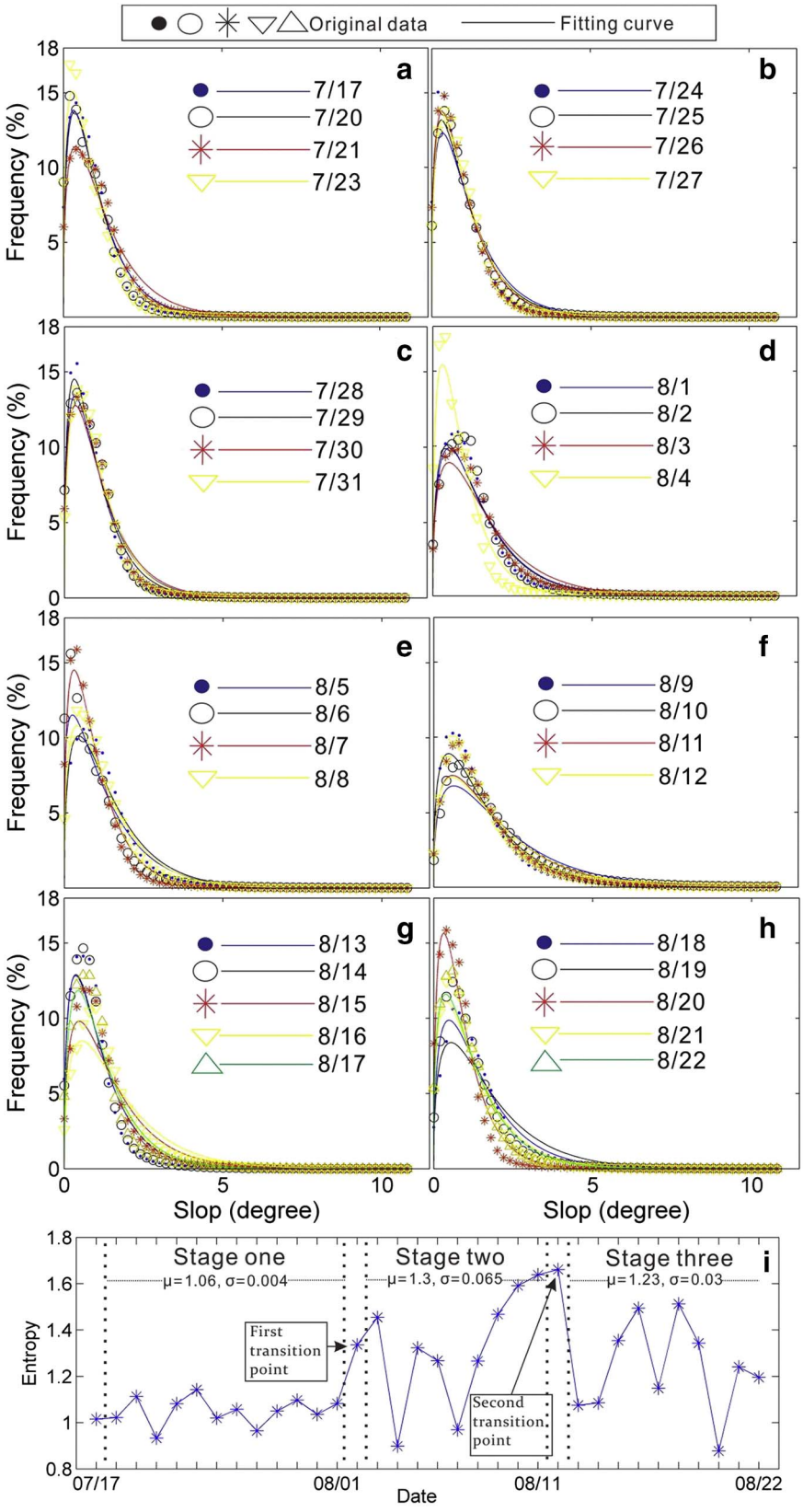

Fig. 10. (a)–(i) Daily frequency distribution of the dominant slope (degree) and the Gamma fitting. (j) Daily entropy of the slope system that was based on the Gamma fitting parameters. The black dashed lines divide the time frame into three stages in agreement with Fig. 6. The μ, σ parameters are the average and variance of the entropy, respectively, in each stage.

coastal dune (black box in Fig. 7c) with an average erosion intensity of approximately − 12 cm, and the second most serious erosion area was located at the seaward MLWNT (blue box in Fig. 7c) with an average erosion density of − 10 cm. The sandbars (two smaller sandbars and one larger sandbar, black dashed box in Fig. 7c), which were close to the MHWNT landward margins, were the third most serious erosion regions with an average change of − 8 cm.

Furthermore, profile P1 shows that the western part of the sandbar crest disappeared after Rammasun. While obvious erosion occurred in the foreshore and dunes, no significant changes were detected in the

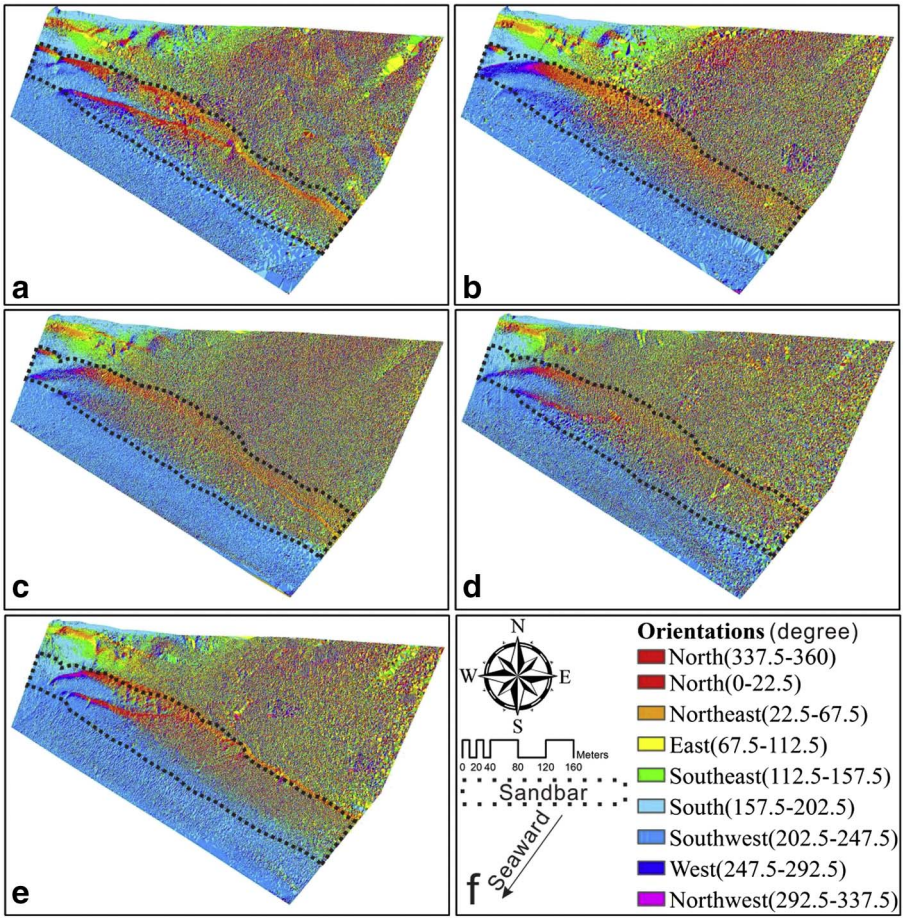

Fig. 11. The dominant aspects of the DEMs for several days. (a) July 17th, (b) July 20th, (c) August 2nd, (d) August 12th, (e) August 22nd, (f) the compass, scale, and legend of (a)–(e).

berm, although a small amount of accretion was generated behind the berm (Fig. 8b). Profile P2 indicates that the winding middle sandbar crest became relatively smooth after Rammasun. Obvious erosion occurred in the foreshore and some accretion appeared behind the sandbar crest. However, there was slight change in the backshore (Fig. 8c). Profile P3 reveals that the eastern sandbar crest and the backshore exhibited no obvious changes; however, an obvious accretion and erosion occurred behind the sandbar crest and in the foreshore, respectively (Fig. 8d). The foreshore of the three profiles experienced completely erosion. However, the accretion/erosion pattern of other sections of the three profiles was quite different, which indicates that various sandbar sections exhibited different behaviors in reaction to Rammasun.

4.3.2. Stages of beach recovery

After typhoon Rammasun, the beach began to recover on July 20th. Through the GRA of the EFDs, the erosion/accretion statistics, dominant slope and aspect statistics, and the three stages of beach recovery with distinct features were obtained (Fig. 9). In Fig. 9a, the GRG variances of stage one (from July 20th to August 1st) and stage three (from August 13th to August 22nd) are 2.5×10^{-5}, which are an order of magnitude smaller than stage two (from August 3rd to August 11th).

During stage one, although GRG was fluctuant, it was always > 0.91, with an average daily net loss of 588 m^3, which suggests that this beach still experienced erosion. In stage one, there was a total volume of 2612 m^3, which indicates variation in either the erosion or accretion (ATEA) (Fig. 9b). Furthermore, the entropy of the dominant slope system indicated a slight variance of 0.4% (Fig. 10j). As a result, the entire beachface appearance was nearly unchanged. The western sandbar crest region indicated a slight accretion, but the sandbar crest did not re-emerge, and the other parts demonstrated no distinct changes in profile P1 (Fig. 8b). Finally, minor erosion occurred in the foreshore of profile P2 and in the sandbar crest and foreshore of profile P3 (Fig. 8c, d).

On August 1st, the beach experienced an extreme accretion; therefore, the GRG of August 2nd drastically decreased from 0.912 to 0.897 (Fig. 9a). At the same time, the entropy of the dominant slope system rapidly increased from 1.08 to 1.32 (Fig. 10i). Accretion occurred in almost the entire area (Figs. 9b and c, 7d, e and f). The accretion degree of the foreshore exceeded that of the backshore. Additionally, the most severe accretion occurred in the larger sandbar (black dashed box in Fig. 7f); therefore, the previous hazy sandbar re-emerged. In profile P1, obvious accretion occurred in most sections except for the dune and the foreshore areas, whereas in profiles P2 and P3, accretion was mainly concentrated in the sandbar crest region (Fig. 8b, c and d).

During stage two, the GRGs showed a relatively severe variation with a variance of 1.1×10^{-4} that ranged from 0.902 to 0.936 (Fig. 9a). Although the ANEA of stage two was -396 m^3 less than that of stage one, the ATEA of stage two reached 3668 m^3, which was nearly 35% greater than the ATEA of the other two stages (Fig. 9b and c). These results imply a reestablishment of the dominant slope system, which can be supported by the changes in the entropy of this system. The entropy variance of stage two reached 6.5%, which means the dominant slope system drastically changed (Fig. 10i). Several infrequent plashes were observed on the beachface via a photo taken on August 3rd (Fig. 3e). However, there was no tidal creek that connected these plashes to the sea. Since no rain was observed on that day, the plash areas can be related to sharp slope changes. In the last day of stage two, the sandbar had a relatively clear outline (Fig. 7g). Clearly, the berm migrated landward, and the foreshore indicated minimal accretion in profile P1 (Fig. 8b). The backshore and sandbar crest experienced erosion in profile P2, whereas the sandbar crest indicated

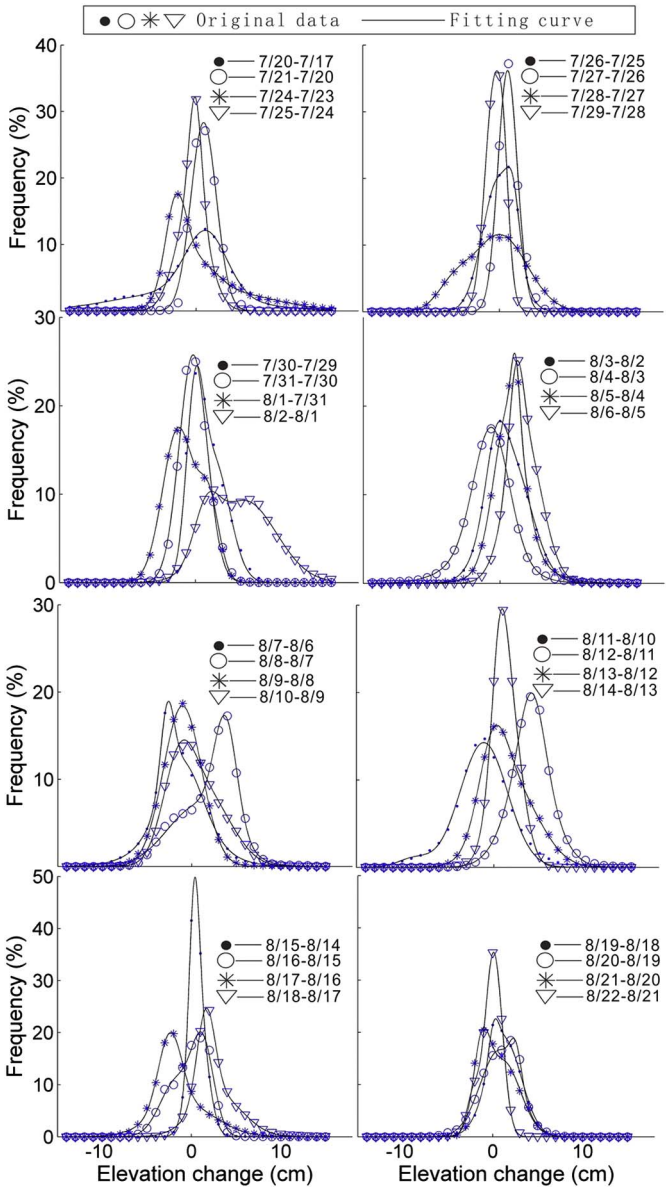

Fig. 12. The frequency distribution of elevation changes and the generalized Gaussian function fitting. The label (for example, "7/21–7/20") in every picture denotes the raster subtraction that was executed between the DEMs from the two days. The curves are fitting curves. The Adjusted-R of all the fitting curves was > 0.99.

some erosion in profile P3 (Fig. 8c, d).

On August 11th, the beach experienced the second extreme accretion; therefore, the GRG on August 12th obviously declined from 0.916 to 0.903 (Fig. 9a). The entropy of the dominant slope system reached a maximum over the entire observation period (Fig. 10i). The entire beachface alternated between erosion and accretion (Fig. 7g, h and i). There was only one strip shaped severe accretion region in the sandbar (black dashed box in Fig. 7i). The berm displayed significant accretion and migrated landward; however, the sandbar crest obviously accreted in profiles P2 and P3 with a slight accretion and erosion in the other parts of profiles P2 and P3 (Fig. 8b, c and d).

During stage three, most GRGs were < 0.9 with small changes. The ANEA of stage three shows that the beach turned into an accretion state (Fig. 9a and b). The entropy of the dominant slope system of stage three indicated that the dominant slope of the beach did not change compared with the condition of stage two because the average value only declined from 1.3 to 1.23, whereas the variance declined from 6.5% to 3%. However, the dominant slope of the beach was more intensive than that of stage one. On August 21st, the penultimate day of our measurement period, two ridges emerged on the beach again (the cyan boxes in Fig. 3f) and the relief surface of the beach was close to the state before Rammasun (Fig. 3c–f). Although the berm suffered slight erosion, it maintained its landward migration in profile P1 (Fig. 8b). The sandbar crest demonstrated slight erosion in profile P2 (Fig. 8c), whereas the sandbar obviously migrated landward in profile P3 (Fig. 8d). Finally, the foreshore of the three profiles recovered to the pre-typhoon beach state.

4.4. The features of erosion/accretion

With high spatial resolution, both the maximum and minimum values of the elevation changes were observed occupied only a small ratio of the total data. Most of the elevation changes occurred in the interval from − 15 cm to 15 cm. The frequency distribution of the elevation changes can be fitted by the generalized Gaussian function (Fig. 12) (Montreuil et al., 2014). While high frequency events were detected on almost the entire beachface, the low frequency events indicated a regional distribution (e.g., Fig. 7c, f, and i).

Through the spatial statistics of the occurrence probability of various erosion and accretion groups, the regional features of the different groups were obtained during the beach recovery process (from July 20th to August 22nd) (Fig. 13). Intense erosion and accretion (− 15 cm to − 6 cm and 6 cm to 15 cm) mainly occurred in the sandbar and foreshore zones (Fig. 13a and f, respectively), whereas slight erosion and accretion (ranging from − 4 cm to 4 cm) were mainly found on the backshore (Fig. 13c and d, respectively). Moderate erosion and accretion (− 6 cm to − 4 cm and 4 cm to 6 cm, Fig. 13b and e, respectively) influenced the entire beach, except in the high value zone, as exhibited in Fig. 13c and d. Particularly, the small dune did not demonstrate a major change during the beach recovery process (Fig. 13), in which both slight erosion and accretion occurred (ranging from − 4 cm to 4 cm). The maximum height of the dune was approximately 0.84 m from July 20th to August 22nd, which was notably lower than the 1.03 m maximum height of the dune on July 17th.

5. Discussion

5.1. Temporal variations in the beach recovery process

According to Morton et al. (1994), the recovery process of this study belongs to the stage of "rapid foreshore accretion", which can be further subdivided into three stages based on the high spatial resolution topographic data. The combination of EFDs, beach volumetric changes, and GRA results indicated that the beach likely experienced weakly stable, choppy, and stable developments, which correspond to the three stages of beach recovery. Although stage one (July 20th–August 1st) and three (August 12th–August 22nd) are relatively stable (lower variance) compared with stage two (August 2nd–August 11th) (Fig. 9a), stage one is characterized by erosion, whereas stage three is characterized by accretion (Fig. 9b). Therefore, there should be a unique stable state for stage one, which is still within the shadow of Rammasun. Moreover, stage two is characterized by the least absolute ANEA and greatest ATEA compared with the other two stages.

Since the chaos state of a system in thermodynamics (Reif, 1965), the amount of information in information theory (Shannon, 1948) and the biodiversity in ecology (Shipley et al., 2006) can be represented by entropy, we prefer it to measure the complexity of dominant slope. In Fig. 10i, the entropy of the dominant slope system maintains a low value and variance in stage one. This result suggests that the dominant slope system, which was created in high energy environment (i.e., Rammasun), was not strongly and immediately changed by external forces. The dominant slope system of stage two revealed the most complicated state (the maximum μ) with the greatest change (the maximum σ), which implies a drastic beach slope reconstruction during

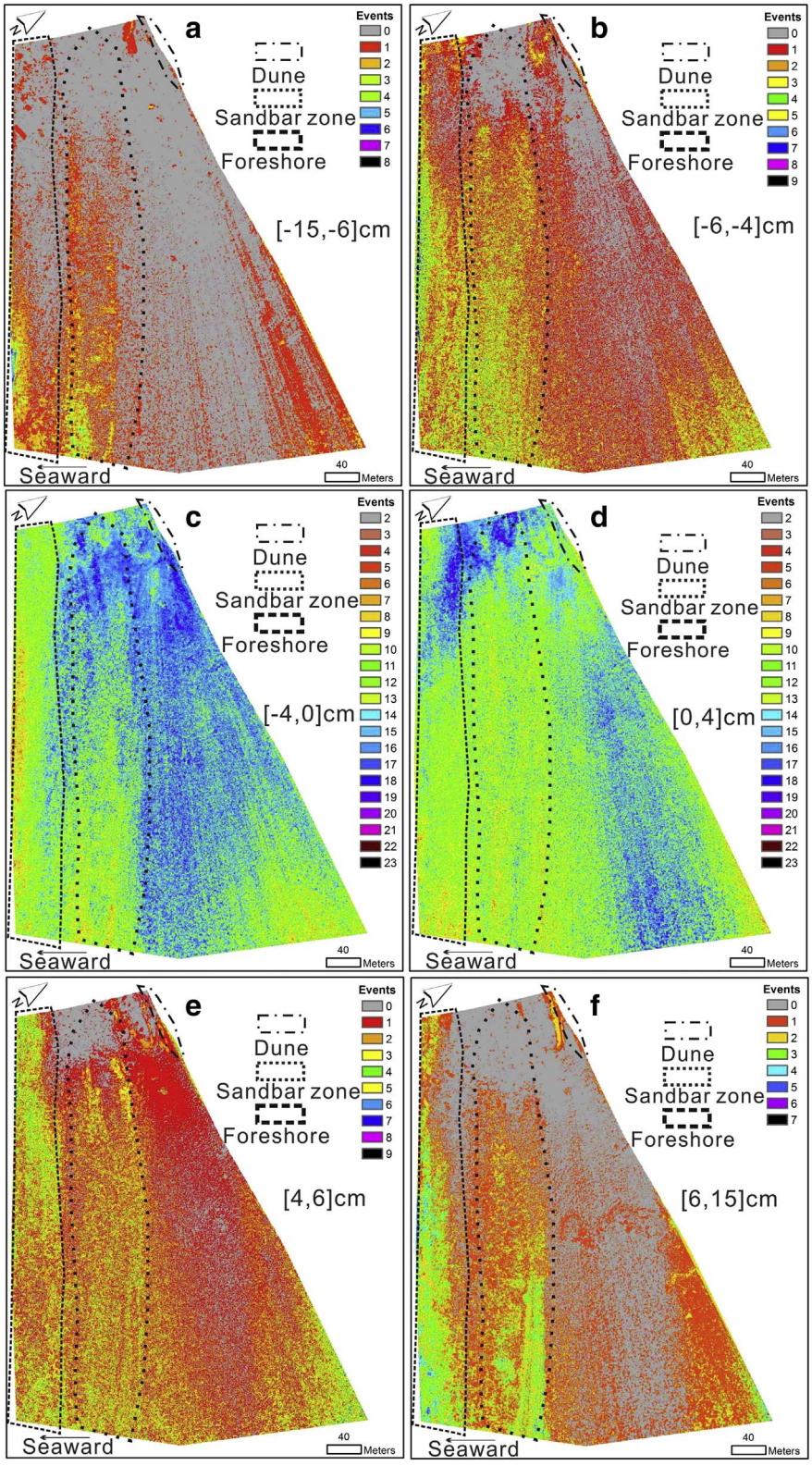

Fig. 13. Occurrence probability of different erosion and accretion groups in space during entire beach recovery process (from July 20th to August 22nd).

stage two. The complexity and variability of the dominant slope declined during stage three after the oscillation in stage two (in terms of smaller average and variance). The slope construction of the beach clearly decayed (Fig. 11).

5.2. Spatial variations in the beach recovery process

The most typical phenomenon of the "rapid foreshore accretion" stage is the reconstitution of the foreshore and sandbar (Dai et al., 2010), which can be found in the spatial distribution of the intense erosion and accretion groups (Fig. 13a and f). Clearly, the sandbar zone divides the beach into two regions: the foreshore and sandbar, which

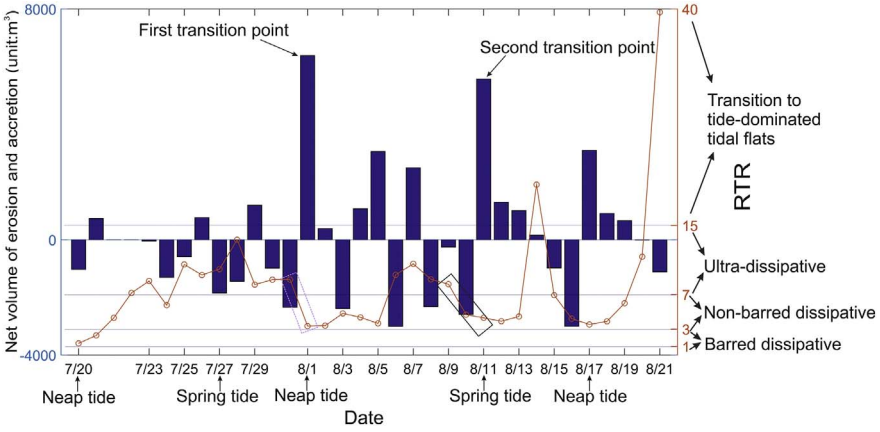

Fig. 14. Beach state based on RTR during the short-term beach recovery process.

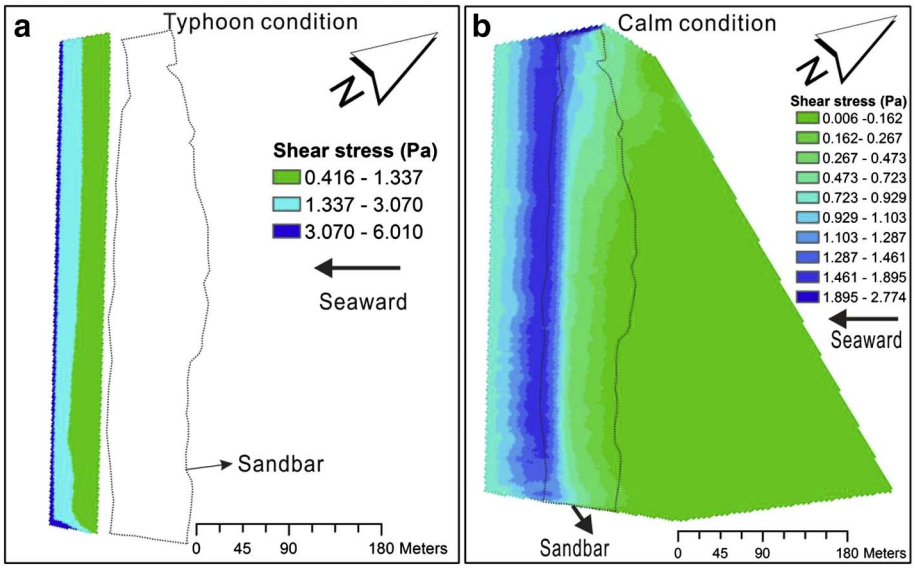

Fig. 15. The distribution of bottom shear stress induced by waves on the beach. (a) Typhoon conditions; (b) calm conditions.

rapidly changed, whereas the backshore maintained a slow changing state. From this view, the sandbar is similar to a double-edged sword, which prevents the backshore from serious erosion that is induced by waves and surges but hinders the sediment transport from the foreshore to the backshore, what means the sandbar reconstruction plays a key role in beach recovery. Furthermore, the dune slightly changed and required an extended time for recovery because of the long term influence of the wind, tide and frequency and magnitude of storm events (Houser et al., 2015).

5.3. *Impacts of the beach state and bottom shear stress on the beach recovery process*

Based on Delft3D model and Eq. (9), the spatial distribution of wave-induced bottom stress over the beach is shown in Fig. 15. The critical shear stress across the beach was approximately 0.162 Pa, which is the minimal shear stress for incipient sediment motion in this area. During Rammasun, the beach was in barred dissipative state ($1 < RTR < 3$; Fig. 14); therefore, offshore transport was presumably dominated by strong offshore directed bottom flow (undertow, Wright et al., 1982). The sandbar protected the inner beachface from serious erosion because of the water level (Figs. 4a, 8); therefore, the relatively steeper foreshore was seriously eroded due to a strong bed shear stress (Figs. 7c and 14a). Additionally, the western part of sandbar crest was destroyed by intensive swash action (Fig. 8b). Furthermore, overwash brought a huge amount of sediment from the foreshore to the backshore by spanning the sandbar, which caused accretion behind the sandbar crest (Fig. 7c; 8c, d; Asbury and Sallenger, 2000; Stockdon et al., 2007). Based on the position of the MWLT, surges could not reach the dune (Fig. 8b); thus, the eroded sediments from the dune were moved to the area behind the berm by wind blowing seaward for an extend period of time (Fig. 8b), which is different from the swash, collision, overwash and inundation regime (Sallenger, 2000; Masselink and Van Heteren, 2014).

Under calm conditions, the beach was mainly in an ultra-dissipative state during stage one; thus, the wide surf zone greatly dissipated the wave energy. At high tide, the surf zone may be intermediate to reflective (Jago and Hardisty, 1984), which is likely to account for the berm migration in stage one (Fig. 8b). The beach state tempestuously changed from ultra-dissipative to non-barred dissipative during the first extreme accretion event (Fig. 14). Due to the impacts of the neap tide of the semi-diurnal tides at Yintan beach, the high water level of one tidal cycle can make the wave influence the sandbar crest. Therefore, the wave asymmetry induced by wave shoaling and breaking could have been responsible for onshore sediment transport to the sandbar crest, which is represented by the obvious accretion in the sandbar crest (Fig. 8c, d). The most intense bottom shear stress occurred in the front of the sandbar (Fig. 15b), which is consistent with the previous studies (e.g., Aagaard et al., 2006). This result can account for the occurrence of intense erosion and accretion groups on the seaward edge of the sandbar crest (Fig. 13a and f). Over the sandbar crest, from sea to land, the bottom shear stress values rapidly decrease landward, which

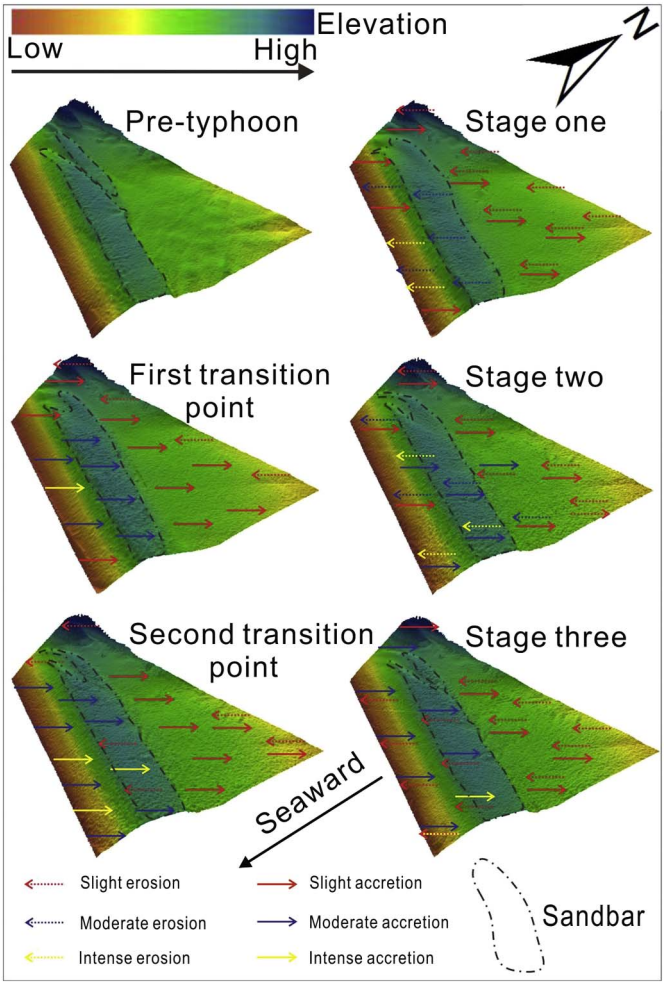

Fig. 16. The diagram of the short-term beach recovery after the typhoon.

indicates that the sediment can be deposited in this area of the beach.

During stage two, the beach state varied from non-barred dissipative state to ultra-dissipative state, with the tide that changed from neap tide to spring tide (Fig. 14). Under lower water level conditions of neap tide, wave breaking may occur closer to the seaward side of the sandbar crest; therefore, slight accretion can be predicted on the foreshore and sandbar crest due to wave asymmetry (Fig. 8b, d). However, under higher water level conditions of spring tide, the low energy waves, which propagate toward the MHWST, could break after the sandbar crest and erode the backshore via undertow (Fig. 8c). Under similar wave conditions, the tide controlled the geomorphic changes during stage two. In the second extreme accretion event, the beach was in non-barred dissipative state, which was close to ultra-dissipative state on August 9th (Fig. 14). In the subsequent stage three, the beach mainly revealed accretion with primarily non-barred dissipative beach states (Fig. 14). Behind the sandbar, the wave-induced bottom shear stress was too small to support sediment suspension.

Apparently, the beach mainly exhibited accretion in non-barred dissipative state, but always presented erosion in ultra-dissipative state. The occurrence of an extreme accretion event was associated with the transition from ultra-dissipative state to non-barred dissipative state. Morton et al. (1994) indicated that the “rapid foreshore accretion” stage (short-term beach recovery) can last for several weeks to one year. Thereafter, the required time for this stage is likely dependent on the beach states. Compared with those of the micro-tidal beach, wave breaking conditions of meso-macro-tidal beach are prominently controlled by the tide, i.e., breaking zone varies with the tidal cycle. The topography, produced by the typhoon, is also of critical significance. For instance, a sandbar crest is similar to a berm in the neap tide, which may turn to a breaker bar during the spring tide (Fig. 8). Therefore, the short-term beach recovery also depends on wave breaking conditions.

5.4. Dynamic equilibrium in beach recovery process

Coco et al. (2014) asserted that beach recovery is controlled by hydrodynamic characteristics, beach type, the presence and location of subaqueous sandbars, spring-neap concurrence and sediment budget. Hence, the beachface that was created by Rammasun played a key role in beach recovery. Specifically, the beach recovery process is that the beach morphology formed in the extreme event (e.g., storm) readapts to ordinary dynamic conditions with landform changes. This process is nonlinear and has two transition jump points (two intense accretion events). From the view of physics, the beach state is regarded as a nonlinear system, which is close to the dynamic equilibrium before Rammasun. In Fig. 16, typhoon Rammasun, which caused intensive wave impact and storm surges, forced the system away from its original dynamic equilibrium in a short time and produced barred dissipative beach state (RTR is close to 1, Fig. 14). Furthermore, the sandbar outline was considerably modified. The system may arrive at a new dynamic equilibrium in the storm (Yates et al., 2009; Dai et al., 2014). After Rammasun, the strong hydrodynamic forces disappeared, but the morphology of the system needed time to approach a new dynamic equilibrium under the hydrodynamic condition of the fair weather, so the system then fell into a weak stable state (stage one) with erosion and minor appearance changes in the sandbar. During this stage, the beach states were mainly ultra-dissipative. Afterwards, the system entered into stage two, which was characterized by significant accretion and noticeable changes in the sandbar morphology. Meanwhile, the beach converted from ultra-dissipative to non-barred dissipative state (dashed box in Fig. 14). In stage two, the system experienced oscillations with dramatic slope changes. In the first half of the stage, the beach state primarily exhibited accretion and was non-barred dissipative beach state, but revealed large-sale erosion with ultra-dissipative beach state in the second half of this stage. At the second transition point, the intense accretion caused the sandbar outline to be increasingly similar in appearance to the pre-Rammasun sandbar. The beach state was close to the transition from ultra-dissipative to non-barred dissipative state (solid box in Fig. 14). Later, in stage three, the system structure gradually became similar to pre-Rammasun state under ordinary hydrodynamic conditions. The foreshore was similar to the pre-typhoon morphology while the sandbar crest moved landward. The beach states were mainly non-barred dissipative with accretion (Fig. 14), whereas the beach erosion was mostly related to ultra-dissipative state. Accordingly, there was an equilibrium state between non-barred dissipative and ultra-dissipative states in Yintan beach.

5.5. Deficiency and prospect

Due to the confidence interval of the beach elevation changes (ranging − 4 cm to 4 cm), the amount of the beach accretion/erosion is not very accurate, but what needs illustration is that the amount of the beach accretion/erosion has clear and correct qualitative meaning due to the frequency of accretion/erosion events following the Gaussian distribution (Fig. 12). For instance, under the condition of ignoring the part of accretion and erosion events between − 4 cm to 4 cm, the net accretion of beach increases when the frequency distribution curve of accretion/erosion events moves toward right (it happens when two frequency curves of accretion/erosion events are compared) because of the frequency increasing in the interval of > 4 cm and the frequency declining in the interval of less than − 4 cm (e.g., the frequency curves of “8/6–8/5” and “8/5–8/4” in Fig. 12). So the frequency distribution of the beach accretion/erosion events following the Gaussian distribution insures that the accretion/erosion results have enough qualitative meaning for supporting these results in this study. However, more

accurate topographic data is necessary for the quantitative analysis for the study of short-term beach evolution in the future.

As shown in many studies (Wright and Short, 1984; Roelvink and Stive, 1989; Russell, 1993; Miles et al., 2006; Coco et al., 2014), wave properties, especially the infragravity waves, are most important for sediment transport and the evolution of beach morphology. The available hydrodynamic data of this study was collected hourly, so it did not satisfy the analysis of infragravity waves. Considering the lack of appropriate hydrodynamic data due to irresistible factors, related work will be conducted after the next fierce typhoon.

6. Conclusions

Based on a 33 days of observation on Yintan beach, the short-term beach recovery process was revealed with high spatial resolution DEMs using a terrestrial laser scanner. During the beach recovery process, there were three stages with two extreme accretion events as the transition points. Paralleling the three stages, Yintan beach experienced successive weakly stable, choppy and stable states, which were dominated by sequential erosion, less erosion and accretion, respectively. The most dramatic geomorphic changes occurred in the sandbar zone, which means that rapid sandbar reconstruction played a key role in the short-term beach recovery process related to the spatial distribution of the wave-induced bottom shear stress. Slight geomorphic changes were detected in the backshore and dunes, which suggests that longer time is required for recovery because of the lack of persistent strong wave activity. The beach states significantly influence the short-term beach recovery through wave breaking condition. The beach recovery process in Yintan shows that the beach approached a new dynamic equilibrium after the high energy environment under calm weather condition.

Acknowledgements

This study was supported with the fundings from the National Natural Science Foundation of China (NSFC) (Grant number: 41376097), the Key Laboratory of Coastal Science and Engineering, Beibu Gulf, Guangxi (2016ZZD01, 2016ZZD02, 2016ZYB01).

References

Aagaard, T., Kroon, A., Andersen, S., Sørensen, R.M., Quartel, S., Vinther, N., 2005. Intertidal beach change during storm conditions; Egmond, The Netherlands. Mar. Geol. 218, 65–80.
Aagaard, T., Hughes, M., Møller-Sørensen, R., Andersen, S., 2006. Hydrodynamics and sediment fluxes across an onshore migrating intertidal bar. J. Coast. Res. 22 (2), 247–259.
Allen, J.R., 2006. Beach erosion as a function of variations in the sediment budget, Sandy Hook, New Jersey, U.S.A. Earth Surf. Process. Landf. 6 (2), 139–150.
Allenbach, K., Garonna, I., Herold, C., Monioudi, I., Giuliani, G., Lehmann, A., Velegrakis, A.F., 2015. Black Sea beaches vulnerability to sea level rise. Environ. Sci. Pol. 46, 95–109.
Angnuureng, D.B., Almar, R., Senechal, N., Castelle, B., Addo, K.A., Marieu, V., Ranasinghe, R., 2017. Shoreline resilience to individual storms and storm clusters on a meso-macrotidal barred beach. Geomorphology 290, 265–276.
Anthony, E.J., 2008. Chapter five sandy beaches and barriers. Mar. Geol. 4, 159–288.
Anthony, E.J., 2013. Storms, shoreface morphodynamics, sand supply, and the accretion and erosion of coastal dune barriers in the southern North Sea. Geomorphology 199, 8–21.
Asbury, H., Sallenger, J., 2000. Storm impact scale for barrier islands. J. Coast. Res. 16 (3), 890–895.
Berry, A.J., Fahey, S., Meyers, N., 2014. Sandy beaches as dynamic refugia: potential barriers to shoreline retreat on the Sunshine Coast, Queensland, Australia. Ocean Coast. Manag. 102, 32–39.
Bird, E.C.F., 1985. Coastline Changes. Wiley & Sons, New York (219 pp.).
Birkemeier, W.A., 1979. The Effects of the 19 December 1977 Coastal Storm on Beaches in North Carolina and New Jersey. 47. Shore Beachpp. 7–15.
Bonte, Y., Levoy, F., 2015. Field experiments of beach scarp erosion during oblique wave, stormy conditions (Normandy, France). Geomorphology 236, 132–147.
Brignone, M., Schiaffino, C.F., Isla, F.I., Ferrari, M., 2012. A system for beach video-monitoring: beachkeeper plus. Comput. Geosci. 49, 53–61.
Castelle, B.O., Turner, I.L., Ruessink, B.G., Tomlinson, R.B., 2007. Impact of storms on beach erosion: broadbeach (Gold Coast, Australia). J. Coast. Res. 23 (1), 534–539.
Chase, A.F., Chase, D.Z., Fisher, C.T., Leisz, S.J., Weishampel, J.F., 2012. Geospatial revolution and remote sensing LiDAR in Mesoamerican archaeology. Proc. Natl. Acad. Sci. U. S. A. 109 (32), 12916–12921.
Coco, G., Senechal, N., Rejas, A., Bryan, K., Capo, S., Parisot, J.P., Brown, J.A., MacMahan, J.H.M., 2014. Beach response to a sequence of extreme storms. Geomorphology 204, 493–501.
Conley, D.C., Beach, R.A., 2003. Cross-shore sediment transport partitioning in the nearshore during a storm event. J. Geophys. Res. 108, 3065.
Costas, S., Alejo, I., Vila-Concejo, A., Nombela, M.A., 2005. Persistence of storm-induced morphology on a modal low-energy beach: a case study from NW-Iberian Peninsula. Mar. Geol. 224, 43–56.
Dai, Z.J., Du, J.Z., Li, C.C., Chen, Z.S., 2007. The configuration of equilibrium beach profile in South China. Geomorphology 86, 441–454.
Dai, Z.J., Liu, J.T., Lei, Y.P., Zhang, X.L., 2010. Patterns of sediment transport pathways on a headland bay beach-Nanwan beach, South China: a case study. J. Coast. Res 26, 1096–1103.
Dai, Z., Liu, J.T., Wei, W., Chen, J.Y., 2014. Detection of the Three Gorges Dam influence on the Changjiang (Yangtze River) submerged delta. Sci Rep 4, 6600.
Del Río, L., Plomaritis, T.A., Benavente, J., Valladares, M., Ribera, P., 2012. Establishing storm thresholds for the Spanish Gulf of Cádiz coast. Geomorphology 143–144, 13–23.
Doucette, J.S., 2000. The distribution of nearshore bedforms and effects on sand suspension on low-energy, micro-tidal beaches in Southwestern Australia. Mar. Geol. 165, 41–61.
Duran, O., Moore, L.J., 2013. Vegetation controls on the maximum size of coastal dunes. Proc. Natl. Acad. Sci. U. S. A. 110, 17217–17222.
Duran Vinent, O., Moore, L.J., 2015. Barrier island bistability induced by biophysical interactions. Nat. Clim. Chang. 5, 158–162.
Fagherazzi, S., Carniello, L., D'Alpaos, L., Defina, A., 2006. Critical bifurcation of shallow microtidal landforms in tidal flats and salt marshes. Proc. Natl. Acad. Sci. U. S. A. 103 (22), 8337–8341.
Ge, Z., Shi, H., Mei, X., Dai, Z., Li, D., 2016. Semi-automatic recognition of marine debris on beaches. Sci Rep 6, 25759.
Hill, H.H., Kelley, J.T., Belknap, D.F., Dickson, S.M., 2004. The effects of storms and storm-generated currents on the sand beaches in southern Maine. Mar. Geol. 210, 149–168.
Houldcroft, C.J., Campbell, C.L., Davenport, I.J., Gurney, R.J., Holden, N., 2005. Measurement of canopy geometry characteristics using LiDAR laser altimetry: a feasibility study. IEEE Trans. Geosci. Remote Sens. 43 (10), 2270–2282.
Houser, C., Wernette, P., Rentschlar, E., Jones, H., Hammond, B., Trimble, S., 2015. Post-storm beach and dune recovery: implications for barrier island resilience. Geomorphology 234, 54–63.
Houston, J.R., Dean, R.G., 2014. Shoreline Change on the East Coast of Florida. J. Coast. Res. 296 (4), 647–660.
Huang, H., Dai, Z.J., Shi, W.Y., Sheng, K., 2001. Deposition characteristics of beach profile in strong-tidal environment - a case study of Yintan, Guangxi during spring. J. Trop. Oceanogr. 30 (4), 71–76.
Ip, W.C., Hu, B.Q., Wong, H., Xia, J., 2009. Applications of grey relational method to river environment quality evaluation in China. J. Hydrol. 379, 284–290.
Jago, C.F., Hardisty, J., 1984. Sedimentology and morphodynamics of a macrotidal beach, Pendine Sands, SW Wales. Mar. Geol. 60, 123–154.
Jiménez, J.A., Sancho-García, A., Bosom, E., Valdemoro, H.I., Guillén, J., 2012. Storm-induced damages along the Catalan coast (NW Mediterranean) during the period 1958–2008. Geomorphology 143, 24–33.
Lee, W.S., Lin, Y.C., 2011. Evaluating and ranking energy performance of office buildings using grey relational analysis. Energy 36, 2551–2556.
Lee, G., Nicholls, R.J., Birkemeier, W.A., 1998. Storm-driven variability of the beach nearshore profile at Duck, North Carolina, USA, 1981–1991. Mar. Geol. 148, 163–177.
Lippmann, T.C., Holman, R.A., 1989. Quantification of sand bar morphology: a video technique based on wave dissipation. J. Geophys. Res. 94 (C1), 995–1011.
Masselink, G., Pattiaratchi, C., 2000. Tidal asymmetry in sediment resuspension on a macrotidal beach in northwestern Australia. Mar. Geol. 163, 257–274.
Masselink, G., Short, A.D., 1993. The effect of tide range on beach morphodynamics and morphology - a conceptual beach model. J. Coast. Res. 9, 785–800.
Masselink, G., Van Heteren, S., 2014. Response of wave-dominated and mixed-energy barriers to storms. Mar. Geol. 352, 321–347.
Masselink, G., Kroon, A., Davidson-Arnott, R.G.D., 2006. Morphodynamics of intertidal bars in wave-dominated coastal settings—a review. Geomorphology 73, 33–49.
Miles, J., Butt, T., Russell, P., 2006. Swash zone sediment dynamics: a comparison of a dissipative and an intermediate beach. Mar. Geol. 231, 181–200.
Montreuil, A., Levoy, F., Bretel, P., Anthony, E.J., 2014. Morphological diversity and complex sediment recirculation on the ebb delta of a macrotidal inlet (Normandy, France): a multiple LiDAR dataset approach. Geomorphology 219, 114–125.
Moore, L.J., Benumof, B.T., Griggs, G.B., 1999. Coastal Erosion Hazards in Santa Cruz and San Diego Counties, California. J. Coast. Res. 28, 121–139 (Special Issue).
Morton, R.A., Paine, J.G., Gibeaut, J.C., 1994. Stages and durations of post-storm beach recovery, southeastern Texas coast, USA. J. Coast. Res. 10 (4), 884–908.
Noshi, Y., Uda, T., Kobayashi, A., Miyahara, S., Serizawa, M., 2015. Beach changes observed in Phan Rang City in Southeast Vietnam. Procedia Eng. 116, 163–170.
Psuty, N.P., Spahn, A., Silveira, T.M., 2013. Sediment budget as a driver for sediment management at plumb beach, New York, USA: vectors of change and impacts. J. Coast. Res. 18 (7), 1–14.
Qi, H., Cai, F., Lei, G., Cao, H., Shi, F., 2010. The response of three main beach types to tropical storms in South China. Mar. Geol. 275 (1–4), 244–254.
Reif, F., 1965. Fundamentals of Statistical and Thermal Physics. McGraw-Hill.
Roelvink, J.A., Stive, M.J.F., 1989. Bar-generating cross-shore flow mechanisms on a

beach. J. Geophys. Res. 94 (C4), 4785–4800.
Rogers, H.E., Swanson, T.W., Stone, J.O., 2012. Long-term shoreline retreat rates on Whidbey Island, Washington, USA. Quat. Res. 78, 315–322.
Russell, P.E., 1993. Mechanisms for beach erosion during storms. Cont. Shelf Res. 13, 1243–1265.
Sallenger Jr., A.H., 2000. Storm impact scale for barrier islands. J. Coast. Res. 890–895.
Salmon, S.A., Bryan, K.R., Coco, G., 2007. The use of video systems to measure run-up on beaches. J. Coast. Res. 50, 211–215.
Saye, S.E., van der Wal, D., Pye, K., Blott, S.J., 2005. Beach–dune morphological relationships and erosion/accretion: an investigation at five sites in England and Wales using LIDAR data. Geomorphology 72, 128–155.
Schwarz, B., 2010. LIDAR: mapping the world in 3D. Nat. Photonics 4, 429–430.
Sedrati, M., Anthony, E.J., 2007. Storm-generated morphological change and longshore sand transport in the intertidal zone of a multi-barred macrotidal beach. Mar. Geol. 244, 209–229.
Semeoshenkova, S., Newton, A., 2015. Overview of erosion and beach quality issues in three Southern European countries: Portugal, Spain and Italy. Ocean Coast. Manag. 118, 12–21.
Semeoshenkova, S., Newton, A., Rojas, M., Piccolo, M.C., Bustos, M.L., Cisneros, M.A.H., Berninsone, L.G., 2016. A combined DPSIR and SAF approach for the adaptive management of beach erosion in Monte Hermoso and Pehuen Co (Argentina). Ocean Coast. Manag In press.
Shannon, C.E., 1948. A mathematical theory of communication. Bell Syst. Tech. J. 27, 379–423.
Shipley, B., Vile, D., Garnier, E., 2006. From plant traits to plant communities: a statistical mechanistic approach to biodiversity. Science 314, 812–814.
Short, A.D., 1991. Macro-meso tidal beach morphodynamics – an overview. J. Coast. Res. 7, 417–436.
Smith, A.M., Guastella, L.A., Botes, Z.A., Bundyn, S.C., Mather, A.A., 2014. Forecasting cyclic coastal erosion on a multi-annual to multi-decadal scale: Southeast African coast. Estuar. Coast. Shelf Sci. 150, 86–91.
Snedden, J.W., Nummedal, D., Amos, A.F., 1988. Storm- and fair-weather combined flow on the Central Texas continental shelf. J. Sediment. Petrol. 58, 580–595.
Stive, M., 2004. How important is global warming for coastal erosion? Clim. Chang. 64, 27–39.
Stockdon, H.F., Sallenger Jr., A.H., Holman, R.A., Howd, P.A., 2007. A simple model for the spatially-variable coastal response to hurricanes. Mar. Geol. 238, 1–20.
Suanez, S., Cariolet, J.M., Cancou, R., Ardhuin, F., Delacourt, C., 2012. Dune recovery after storm erosion on a high-energy beach: Vougot Beach, Brittany (France). Geomorphology 139–140, 16–33.
Tang, Y.S., Ma, S.C., Chung, L.K., 1995. Determination of optimal cutting parameters in wire electrical discharge machining. Int J Mach Tool Manu 35 (12), 1693–1701.
Tang, Z., Xu, L., Jiang, W., Hirsh, A., 2013. Capturing LiDAR-derived hydrologic spatial parameters to evaluate playa wetlands. J. Am. Water Resour. Assoc. 50 (1), 234–245.
Tang, Z., Gu, Y., Dai, Z., Li, Y., Lagrange, T., Bishop, A., Drahota, J., 2015. Examining playa wetland inundation conditions for national wetland inventory, soil survey geographic database, and LiDAR data. Wetlands 35 (4), 1–14.
Third Institute of Oceanography, State Oceanic Administration, 2010. Coast Erosion Assessment and Control: The Final Report, Chinese Offshore Investigation and Assessment. pp. 39–59.
Wang, P., Kirby, J.H., Haber, J.D., Horwitz, M.H., Knorr, P.O., Krock, J.R., 2006. Morphological and sedimentological impacts of hurricane Ivan and immediate post-storm beach recovery along the Northwestern Florida barrier-island coasts. J. Coast. Res. 6, 1382–1402.
Woodroffe, C.D., 2007. The natural resilience of coastal systems: primary concepts. In: McFadden, L., Penning-Rowsell, E., Nicholls, R.J. (Eds.), Managing Coastal Vulnerability. Elsevier, Amsterdam, pp. 45–60.
Woolard, J.W., Colby, J.D., 2002. Spatial characterization, resolution, and volumetric change of coastal dunes using airborne LIDAR: Cape Hatteras, North Carolina. Geomorphology 48, 269–287.
Wright, L.D., Short, A.D., 1984. Morphodynamic variablity of surf zones and beaches: a synthesis. Mar. Geol. 56, 93–118.
Wright, L.D., Chappell, J., Thom, B.G., Bradshaw, M.P., Cowell, P., 1979. Morphodynamics of reflective and dissipative beach and inshore systems: Southeastern Australia. Mar. Geol. 32, 105–140.
Wright, L.D., Guza, R.T., Short, A.D., 1982. Dynamics of a high energy dissipative surf zone. Mar. Geol. 45, 41–62.
Wright, L.D., Boon, J.D., Kim, S.C., List, J.H., 1991. Modes of cross-shore sediment transport on the shoreface of the Middle Atlantic Bight. Mar. Geol. 96, 19–51.
Xu, J., Sheng, G.P., Luo, H.W., Fang, F., Li, W.W., Zeng, R.J., Tong, Z.H., Yu, H.Q., 2011. Evaluating the influence of process parameters on soluble microbial products formation using response surface methodology coupled with grey relational analysis. Water Res. 45, 674–680.
Yang, X., Strahler, A.H., Schaaf, C.B., Jupp, D.L.B., Yao, T., Zhao, F., Wang, Z., Culvenor, D.S., Newnham, G.J., Lovell, J.L., Dubayah, R.O., Woodcock, C.E., Ni-Meister, W., 2013. Three-dimensional forest reconstruction and structural parameter retrievals using a terrestrial full-waveform LIDAR instrument (Echidna®). Remote Sens. Environ. 135, 36–51.
Yates, M.L., Guza, R.T., O'Reilly, W.C., 2009. Equilibrium shoreline response: observations and modelling. J. Geophys. Res. 114, C09014.
Yoshikawa, S., Nemoto, K., 2010. Seasonal variations of sediment transport to a canyon and coastal erosion along the Shimizu coast, Suruga Bay, Japan. Mar. Geol. 271, 165–176.
Zhang, K., Douglas, B.C., Leatherman, S.P., 2002. Do storms cause long-term beach erosion along the US East Barrier Coast. J. Geol. 110, 493–502.
Zhang, K., Douglas, B.C., Leatherman, S.P., 2004. Global warming and coastal erosion. Clim. Chang. 64, 41–58.